Modeling and H-Infinity Loop Shaping Control of a Vertical Takeoff and Landing Drone

by

Vignesh Raghuraman

A Thesis Presented in Partial Fulfillment
of the Requirements for the Degree
Master of Science

Approved April 2018 by the
Graduate Supervisory Committee:

Konstantinos Tsakalis, Chair
Armando Rodriguez
Sze Zheng Yong

ARIZONA STATE UNIVERSITY

May 2018

ABSTRACT

VTOL drones were designed and built at the beginning of the 20th century for military applications due to easy take-off and landing operations. Many companies like Lockheed, Convair, NASA and Bell Labs built their own aircrafts but only a few from them came in to the market. Usually, flight automation starts from first principles modeling which helps in the controller design and dynamic analysis of the system.

In this project, a VTOL drone with a shape similar to a Convair XFY-1 is studied and the primary focus is stabilizing and controlling the flight path of the drone in its hover and horizontal flying modes. The model of the plane is obtained using first principles modeling and controllers are designed to stabilize the yaw, pitch and roll rotational motions.

The plane is modeled for its yaw, pitch and roll rotational motions. Subsequently, the rotational dynamics of the system are linearized about the hover flying mode, hover to horizontal flying mode, horizontal flying mode, horizontal to hover flying mode for ease of implementation of linear control design techniques. The controllers are designed based on an H_∞ loop shaping procedure and the results are verified on the actual nonlinear model for the stability of the closed loop system about hover flying, hover to horizontal transition flying, horizontal flying, horizontal to hover transition flying. An experiment is conducted to study the dynamics of the motor by recording the PWM input to the electronic speed controller as input and the rotational speed of the motor as output. A theoretical study is also done to study the thrust generated by the propellers for lift, slipstream velocity analysis, torques acting on the system for various thrust profiles.

DEDICATION

Dedicated to my father Mr. Raghuraman Natarajan and my mother Ms. Sampathkumari Venkataramanan

ACKNOWLEDGMENTS

I would like to thank many people who have advised, guided and inspired me to complete this thesis. First, I would like to express my heartful gratitude to my advisor Dr. Konstantinos Tsakalis. I took his Computer controlled systems, Nonlinear systems, Adaptive control systems and they taught me the fundamentals as well as the advanced topics in Control Systems. His lectures were pivotal in helping me understand the subject and tremendously aiding my research. I am very thankful to him for giving me an opportunity to work on this project which very much exposed me to the practical implementation of theoretical ideas. Secondly I would like to thank Dr.Armando Rodriguez. I took Prof Rodriguez's linear systems theory, Feedback systems and Multi-Variable control systems which really helped me in addition to the other classes. All of his classes helped me in the practical implementation of controller design and was greatly helpful in my research. I would also like to thank Prof. Raja Ayyanar, Prof. Spanias and Prof. Cochran who also provided me knowledge in the area of power electronics and signal processing which was very helpful.

I would also like to thank my labmates, Md Shafique, Rakesh Joshi, Vishwam Aggarwal and Darpan Saha for helping me in this project. Special thanks to Md Shafique, Rakesh Joshi for enlightening me with the concepts in Hardware design and implementation. I would also like to thank Vishwam for helping me with the concepts associated with the hardware implementation of the drone. I would also like to thank my friends Vignesh Namasivayam, Blas Hernandez, Uday Shankar and Dheeraj who helped me to test the plane in the lawns. I would also like to thank my friend Arun Srivatsa Ramesh for me giving me ideas during our discussions about the plane.

Great appreciation to my parents who have supported me financially and emotionally through my masters degree. I would also like thank my cousins Raman Shivaram

and Vivekananda Raman who also supported me financially and emotionally through my masters degree. Without them, I would never had the chance to pursue my masters degree.

TABLE OF CONTENTS

CHAPTER Page

LIST OF FIGURES

Figure Page

Figure Page

Chapter 1

INTRODUCTION

1.1 Overview

The VTOL planes came in to existence in the beginning of the 20th century and Leonardo da Vinci had imagined about them in his writings. Many companies started building vertical take-off and landing planes during that time owing to their ease in take-off and landing operations. They are widely used in military, surveying and geographical mapping applications. Recently, Boeing developed an unmanned electric VTOL plane which would refuel aircrafts for the US Navy. Other companies like Uber and Aurora flight sciences are very much interested to do research on the VTOL drones in their operation for passenger and cargo delivery purposes. The advantages of VTOL drones is their ability to take off and land from a small amount of space almost everywhere along with switching between hover and horizontal flying mode. They are usually small in size and can be operated in a congested environment. Due to the advancement of power electronics and navigation systems, highly powerful and efficient motors, and sophisticated inertial measurement units can be installed in the drones giving more flexibility with respect to weight constraints.

Unfortunately, on the other side, VTOL drones are vulnerable to environmental factors such as wind and the complexity in the dynamics during switching between the hovering and horizontal flying mode makes them difficult to operate. So, it is critical for the control system to stabilize the complex dynamics and as well compensate for the external disturbances by rejecting them for a stable flight. The control system must also guarantee robustness with respect to uncertainties in the modeling, drone

operation and external disturbances.

A good control system is necessary to operate the plane for commercial uses. While doing a control system design, there are time domain and frequency domain performance specifications that we need to target. In the time domain performance measures, we have to achieve good performances in rise time, peak time, overshoot and settling time parameters. The rise time, peak time for the control system should be small and the drone should be able to reach its reference input quickly. There should not be big overshoots causing oscillations and hence destabilizing the closed loop system. Thinking about it in a real perspective, the drone might destabilize and result in the loss of property and lives. From the frequency domain perspective, the bandwidth of the closed loop system should be a large value for a fast response with good stability margins. The transient performance and the steady state performance of the closed loop is also important for easy maneuvering and the stability of the drone. The transient performance is the ability of the drone to reach the reference input quickly and not exhibiting oscillations. The transient performance is critical for the drone to reach its reference value quickly during take-off and stabilize in the presence of external disturbances. The drone must reach its steady state value to avoid drift because of steady state error.

The usual way of control system design starts from modeling the system based on its parameters. The model of the system can be obtained from the first principles theory or by system identification techniques. In our case, since the plane is unstable in the open loop operation, first principles modeling is a good way to obtain the model of the system. The non-linear dynamics of the system is to be known to do the switching between the hover flying and horizontal flying considering the complexity involved. For this project, the non-linear model of the drone is obtained in the form of differential equations from first principles theory. By linearizing the non-linear

equations about hover flying, hover to horizontal transition flying, horizontal flying and horizontal to hover flying, the controller design technique is simplified with ease in implementation. The controller formulated will stabilize the drone about hover and horizontal flying. Since, there is a critical stall velocity associated with the horizontal flying which creates a turbulent air flow over the wings, the drone must be operated above that threshold. There are also actuator saturations in control inputs varying with the speed of rotation of the motors to be taken in to account during the closed loop implementation of the system. The flight of the drone about hover flying, horizontal flying, hover to horizontal transition, horizontal to hover transition is proposed in this thesis for the operation of the drone.

1.2 Literature Review

For the purpose of implementing the flight of the plane, the model of the drone need to be obtained. The modeling of the drone can be done by a system identification technique or by a physics based first principles modeling. To do a first principles modeling, the parameters of the system need to be computed using theorems from physics. The moment of inertia of the drone need to be computed and it is explained in [43] by Muliadi et.al. The moment of inertia in a rotational motion is analogous to mass in a linear motion. The moment of inertia is the resistance of the drone towards the rotational motion on the application of torque input. Greater the moment of inertia, greater is the resistance shown by the system towards the torque applied.

With the moment of inertia computed, the center of mass also needs to be determined which will be the center of rotation. The non-linear equations of motion of the system are computed as shown in [12] by Peet. The differential equations of motion govern the yaw, pitch and roll rotations with the torque inputs acting on the system. The equilibrium points of the system can be computed from the non-linear differential

equation as shown by Khalil in [8]. This would help in knowing the stable operating point of the system for a real flight operation. For ease in control implementation, the non-linear equations of motion can be linearized as shown in [5] by Tsakalis et.al, [8] by Khalil and in [9] by Mcruer et.al. The linearized matrices in state-space are converted to transfer functions about hover flying, 6 equidistant operating points in hover to horizontal flying, horizontal flying and 6 more equidistant operating points in horizontal to hover flying. The linearized models of the system are used for controller design based on the targeted design objectives in target loop shape, weighting functions, settling time, peak time, bandwidth etc.

The controller design can be done by different techniques like PID loop shaping control as shown in [45] by Tsakalis et.al, linear quadratic regulator as shown in [3] by Zhou et.al, H_∞ loop shaping control by Stoorvogel in [6], McFarlane in [10]. Non-linear control techniques such as the back-stepping control, gain scheduling control, feedback linearization, sliding mode control can also be designed considering the non-linearities in the system and guarantee robustness in closed loop control as shown in [8] by Khalil. A robust H_∞ control for a nonlinear system like non-isothermal CSTR is presented by Sana et.al in [29]. An another application of nonlinear H_∞ control for the rotary pendulum is presented in [30] by Rigatos et.al. A non-linear H_∞ controller can be synthesized based on L_2 gain and dissipativity concepts which requires solving of a Hamilton- Jacobi- Isaacs equation is presented in [31] by Garcia et.al. The non-linear H_∞ controller in comparison with the linear version allows for larger perturbations from the trim condition and delays control degradation and risk of instability. The stability and the operation of a nonlinear robotic manipulator is done by the use of model predictive controller and a H_∞controller as presented in [32] by Ullah et.al. An automation technique has also been presented by Rafaila et.al based on H_∞ control technique for the different maneuvers with a vehicle steering

during the motion of a ground vehicle. A structured H_∞ control based on classical parameters has also been presented by Tapia et.al for the vega launch vehicle in [34]. Selection of weighting functions can be done based on particle swarm optimization technique for the H_∞ controller design to the robust control of brush-less DC motor is presented in [35] by Vinida et.al. This novel strategy is a very good technique to reduce the peaks in the sensitivity and complementary sensitivity function which is directly related to the performance of closed loop reference tracking, disturbance rejection, insensitivity to modeling errors and noise. An autonomous VTOL design for the quad-copter using input to state linearization and fuzzy Takagi Sugeno has been presented by Chalidia et.al in [36]. Demitri et.al discusses about a technique to determine real time wind speed and direction during the flight of a VTOL tail-sitter by using on-board sensors like inertial measurement unit(IMU), global positioning system(GPS) and a magnetometer. Using the data from these sensors, a kalman filter is implemented to estimate the wind parameters. The design and control of an indoor micro quad rotor is discussed by Bouabdallah et.al where the drone is modeled and controllers are designed to test the flight of the plane in real-time. The development and experimental verification of a hybrid vertical take-off and landing(VTOL) is presented by Gu et.al in [13] where the development of the UAV with on-board devices integration, ground station support and long distance communication is presented. For the same design, aerodynamic analysis, mechanical design and controller development is presented in [13]. When the dynamics of a complex system are coupled with respect to multiple inputs, then decoupling the system is necessary to implement single input single output control which is presented by Pappa et.al in [22]. The decoupling of the binary distillation column with the use of state space de-couplers is shown in [22] and they are also compared with the conventional decoupler. The comparison of the state-space decoupler to that of conventional decoupler is also dis-

cussed in [22]. A sliding mode control can also be done for a nonlinear system and is implemented with a de-coupler for a multi-variable coupled tank process as presented in [23] by B.J. Parvati et.al. A dynamic decoupling design for a class of linear multi-variable system is presented in [25] by Devi et.al. A dynamic state feedback based decoupler is designed for a MIMO system and the robustness of the closed loop is tested as presented by Devi et.al in [25]. A dynamic state feedback decoupler which is the extension of the static feedback decoupler can also be implemented for a multiple input multiple output system as presented by Devi et.al in [26]. The application of the decoupler in the chemical industry is presented in [27] by Sundari et.al where a de-coupler based PI control strategy is implemented for a CSTR and the stabilizing effect of the controller is shown.

1.3 Thesis Organization

This thesis is organized in seven chapters. In chapter 2, first principles modeling technique is presented. The methods used to compute the moment of inertia tensor and the non-linear differential equations of motion are also presented. In chapter 3, the linearized dynamical model of the hover flying mode, transition from hover to horizontal flying mode, horizontal flying mode and transition from horizontal to hover flying mode are also presented. Chapter 4 contains the methods for controller design namely PID loop shaping controller design, linear quadratic regulator and H_∞ loop shaping controller design. Chapter 5 consists of system modeling, controller design and theoretical results. The VTOL drone studied in the project is explained along with theoretical results from system modeling, controller design, motor dynamical model, slipstream velocity analysis, thrust profile analysis and torque analysis. In chapter 6, the simulation results are presented. The flight simulation of the hover flying mode, hover to horizontal flying transition mode, horizontal flying mode and

horizontal to hover flying transition mode are shown. In chapter 7, the conclusion and the future work of this project are presented.

Chapter 2

FIRST PRINCIPLES MODELING

2.1 Introduction

In this chapter, the method used for computing the dynamical model of the system by first principles model is presented which is elaborated in (28),(12). The discussion begins by computing the mass moment of inertia tensor of the system. Next, the non-linear differential equations of motion of the system based on the principle of conservation of angular momentum is presented. Next, the theory behind computing the dynamical model of the motor based on theory as well from experiments are shown. In the later section of the chapter, slipstream velocity generation based on the speed of rotation of propellers is explained. Next, the thrust force generated by the propellers is explained. Finally, the control inputs acting on the system which influence the rotational dynamics of the system are elaborated.

2.2 Moment of Inertia

Mass moment of inertia of a rigid body is a tensor that determines the amount of torque needed to produce a desired angular acceleration about a particular rotational axis. The mass moment of inertia in a rotational motion is analogous to mass in a linear motion. The units of moment of inertia is kgm^2 in SI units and pound-squarefeet in imperial units. The moment of inertia of a point mass is the mass times the square of the perpendicular distance from the rotation axis. For a rigid composite system, it is the sum of the moments of inertias of the subsystems. One of the other definitions is that, the moment of inertia is the second moment of mass with respect

to distance from an axis r, integrating over the entire mass of the body(Q). For a rigid body, the moment of inertia about a rotational axis is given by the formula (2.1).

$$I = \int_Q r^2 dm \tag{2.1}$$

For rigid bodies that can rotate in 3 dimensional axes, their moments are described by a symmetric 3×3 matrix which is called the moment of inertia tensor. The diagonal elements of the moment of inertia tensor represent the moments about the x, y and z axis respectively. The off-diagonal elements represent the moments about the x-y axis, x-z axis, y-x axis, y-z axis, z-x axis, z-y axis respectively. The moment of inertia tensor(I) is represented as

$$I = \begin{bmatrix} I_{xx} & I_{xy} & I_{xz} \\ I_{yx} & I_{yy} & I_{yz} \\ I_{zx} & I_{zy} & I_{zz} \end{bmatrix}$$

The diagonal elements of the matrix can be computed using the equation (2.2).

$$\begin{aligned} I_{xx} &= \int_m (y'^2 + z'^2) dm \\ I_{yy} &= \int_m (x'^2 + z'^2) dm \\ I_{zz} &= \int_m (x'^2 + y'^2) dm \end{aligned} \tag{2.2}$$

The off-diagonal elements of the inertia tensor are called the products of inertia and are given by the equations (2.3), (2.4) and (2.5).

$$I_{xy} = I_{yx} = \int_m (x'y') dm \tag{2.3}$$

$$I_{xz} = I_{zx} = \int_m (x'z') dm \tag{2.4}$$

$$I_{yz} = I_{zy} = \int_m (y'z')dm \tag{2.5}$$

It follows from the definition of the products of inertia, that the moment of inertia tensors are always symmetric. For a general three-dimensional body, 3 mutually orthogonal axes (x, y, z coordinate system) can be determined and the inertia matrix takes a diagonal form with the products of inertia being zero. We would like to compute the inertia tensor about these axes to formulate a problem statement. When a rotation is considered about only one of the 3 rotational axes, the angular momentum vector is parallel to the angular velocity vector. For symmetric bodies, it is easy to identify which of these axes are the principal axis. However, for a rigid body with an irregular shape, it is difficult to determine the principal axes of rotation. But, for a rigid body that is symmetric about a particular axis, then the products of inertia are zero and the principal axes can be identified. For example, if a body is symmetric with respect to the plane $y' = 0$ then, we will have

$$I_{y'x'} = I_{x'y'} = I_{y'z'} = I_{z'y'} = 0$$

and y will be a principal axis as shown in figure 2.1. This result can be shown from the definition of products of inertia.

The integral for, say, $I_{y'x'}$ can be decomposed in to two integrals for the two halves of the body at either side of the plane $y = 0$. The integrand on one half, $y'x'$ will be equal in magnitude and opposite in sign to the integrand on the other half since y' is changing sign. Therefore, the integrals over the two halves will cancel each other and the product of inertia I_{yx} will be zero. Also, if the body is symmetric with respect to two planes through the center of mass which are orthogonal to the principal axis, then the cross terms of the inertia tensor are zero ($I_{yx} = I_{yz} = I_{zx} = 0$) and the inertia tensor is diagonal. For a composite system, the inertia tensor of the individual components are computed separately and the sum of them is the inertia tensor of the

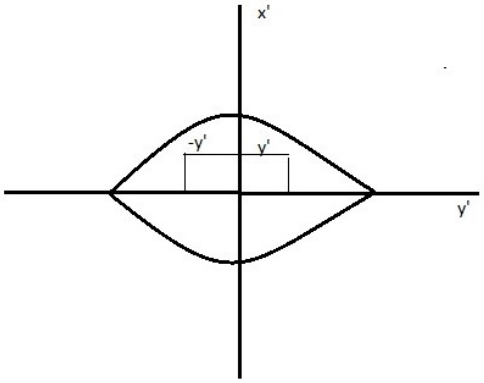

Figure 2.1: A Symmetric Rigid Body about the Axis Y' = 0

system as explained earlier. However, in that case the inertia tensor of the individual components are generally computed about the axis passing through their own center of mass. Hence, there arises a scenario to calculate the inertia tensor about the axis passing through the center of mass of the composite system. The inertia tensor can be transformed about the axes passing through the center of mass of the system by the parallel axis theorem. Parallel axis theorem states that the moment of inertia of a body about an axis parallel to the axis passing through the center of mass is the sum of the moment of inertia about the axis passing through the center of mass and the product of the body's mass with the square of the distance between the two axis.

$$I = I_{cm} + md^2 \tag{2.6}$$

The parallel axis theorem can be extended to a 3-dimensional rigid body as shown below. Consider the figure shown below where the inertia tensor is known about x, y, z axis.

We are interested in finding the inertia tensor about the new axis x, y, z parallel

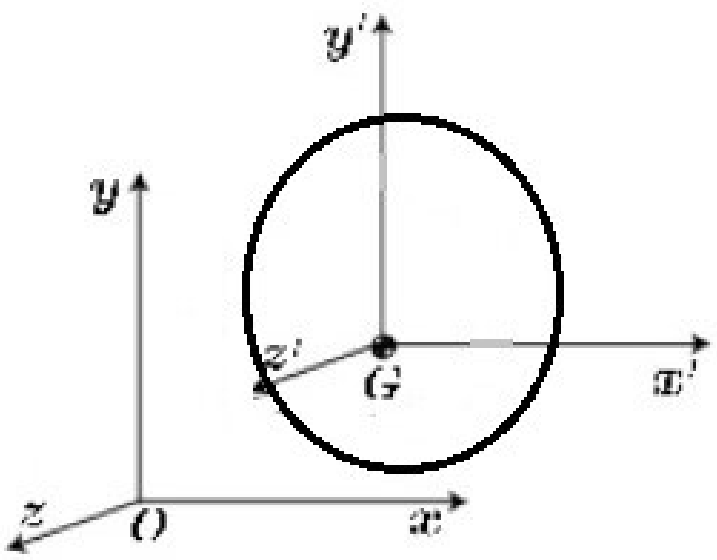

Figure 2.2: Moment of Inertia about a Different Rotational Axis

to the x, y, z axis. We can say that,

$$(I_{xx})_O = \int_m (y^2 + z^2)dm = \int_m ((y_G + y')^2 + (z_G + z')^2)dm \tag{2.7}$$

$$(I_{xx})_O = \int_m (y'^2 + z'^2) + 2y_G \int_m y'dm + 2z_G \int_m z'dm + ({y_G}^2 + {z_G}^2) \int_m dm \tag{2.8}$$

$$(I_{xx})_O = I_{xx} + m((y_G)^2 + (z_G)^2) \tag{2.9}$$

Since the y and z axis are the coordinates relative to the center of mass and hence the integrals over their body are zero. This makes the terms $\int_m y'dm$ and $\int_m z'dm$ equal to zero. Similarly, we can get the inertia tensor about the y-axis passing through O and the z-axis passing through O.

$$(I_{yy})_O = I_{yy} + m(x_G^2 + z_G^2), (I_{zz})_O = I_{zz} + m(x_G^2 + y_G^2) \tag{2.10}$$

The non-diagonal terms of the inertia tensor are given by:

$$(I_{xy})_O = (I_{yx})_O = I_{xy} + mx_G y_G, (I_{xz})_O = (I_{zx})_O = I_{xz} + mx_G z_G \tag{2.11}$$

$$(I_{yz})_O = (I_{zy})_O = I_{yz} + my_G z_G \tag{2.12}$$

The center of mass of any object is a critical point in the body about which the entire mass of the object is assumed to be acting. For a single rigid body, the center of mass is fixed in relation to the body and has uniform density, then it is located in the centroid of the body. The center of mass of a two-particle system P_1 and P_2 with masses m_1 and m_2 is given by the formula in (2.13).

$$R = \frac{(m_1 r_1 + m_2 r_2)}{m_1 + m_2} \tag{2.13}$$

The center of mass of a body with an axis of symmetry and constant density will lie on its axis of symmetry. The center of mass of a body can be experimentally determined by suspending the body from two points and to drop plumb lines from the suspension points. For a complex shaped body, the body can be divided in to smaller elementary shaped masses whose center of mass can be determined easily. If the total mass of the body and the center of mass can be determined for each of the smaller masses, then the weighted average of the centers is the center of mass of the body as shown in the equation (2.14).

$$C_f = \frac{w_1 c_1 + w_2 c_2 + \cdots w_n c_n}{w_1 + w_2 + \cdots w_n} \tag{2.14}$$

The exact co-ordinates of the center of mass of a 3-dimensional rigid body can also be determined experimentally by supporting the object at three points and measuring the forces F_1, F_2, F_3 that resist the weight of the object at these 3 points. Let $W = -W\hat{k}$, where $\hat{k}$ is the unit vector in the vertical direction. Let p_1 , p_2, p_3 be the position co-ordinates of the support points. Then the co-ordinates of the center of mass(C) will satisfy the below condition such that the resultant torque is zero. Let τ be the torque acting on the system. Expressing the torque acting on the system we

get,

$$\tau = (r_1 - C) \times F_1 + (r_2 - C) \times F_2 + (r_3 - C) \times F_3 = 0$$

$$or \tag{2.15}$$

$$C \times (-W\hat{k}) = r_1 \times F_1 + r_2 \times F_2 + r_3 \times F_3$$

.

Simplifying the equation in (2.15), we get equation (2.16) by which the center of mass can be computed.

$$C^* = \frac{\hat{k}}{W} \times (r_1 \times F_1 + r_2 \times F_2 + r_3 \times F_3) \tag{2.16}$$

The center of mass lies on the vertical line V which is given by the equation (2.17).

$$V(t) = C^* + t\hat{k} \tag{2.17}$$

The exact co-ordinates of the center of mass can be determined by performing the above experiment with the object positioned in a different orientation so that these forces can be measured for two different horizontal planes through the object. The intersection of the lines V_1 and V_2 from both the experiments will be the center of mass of the body.

2.3 Nonlinear Equations of Motion

There are 3 rotational motions about the fundamental axes namely the roll, pitch and yaw rotations. Newton's second law states that the moments/torque acting on a rigid body is the sum of the components acting separately on the body as shown by the equation (2.18).

$$\vec{M} = \sum_i \vec{M_i} = \frac{d}{dt}\vec{H} \tag{2.18}$$

where

$$\vec{H} = I\vec{w_I} \tag{2.19}$$

and I is the moment of inertia tensor expressed as

$$I = \begin{bmatrix} I_{xx} & -I_{xy} & -I_{xz} \\ -I_{yx} & I_{yy} & -I_{yz} \\ -I_{zx} & -I_{zy} & -I_{zz} \end{bmatrix}$$

w_I is the angular rotation vector of the body defined in the inertial frame and is expressed below.

$$w_I = \begin{bmatrix} p_I \\ q_I \\ r_I \end{bmatrix}$$

where p_I is the angular rotation about the x-axis, q_I is the angular rotation about the y-axis, r_I is the angular rotation about the z-axis.

Hence we compute the angular momentum as shown in (2.20).

$$\begin{bmatrix} H_x \\ H_y \\ H_z \end{bmatrix} = \begin{bmatrix} I_{xx} & -I_{xy} & -I_{xz} \\ -I_{yx} & I_{yy} & -I_{yz} \\ -I_{zx} & -I_{zy} & -I_{zz} \end{bmatrix} \begin{bmatrix} p_I \\ q_I \\ r_I \end{bmatrix} \tag{2.20}$$

If the body-fixed frame is rotating with a rotation vector $\vec{w}$, then for any vector $\vec{v}$, (2.21) holds good.

$$\frac{d\vec{a}}{dt}\Big|_I = \frac{d\vec{a}}{dt}\Big|_B + \vec{w} \times \vec{a}. \tag{2.21}$$

Specifically for newton's second law, we can say that

$$\vec{M} = \frac{d\vec{H}}{dt}\Big|_B + (\vec{w} \times \vec{H}) \tag{2.22}$$

Using the equations in (2.20) and (2.22) we get,

$$\begin{bmatrix} L \\ M \\ N \end{bmatrix} = \begin{bmatrix} I_{xx} & -I_{xy} & -I_{xz} \\ -I_{yx} & I_{yy} & -I_{yz} \\ -I_{zx} & -I_{zy} & -I_{zz} \end{bmatrix} \begin{bmatrix} \dot{p} \\ \dot{q} \\ \dot{r} \end{bmatrix} + \vec{w} \begin{bmatrix} I_{xx} & -I_{xy} & -I_{xz} \\ -I_{yx} & I_{yy} & -I_{yz} \\ -I_{zx} & -I_{zy} & -I_{zz} \end{bmatrix} \begin{bmatrix} p \\ q \\ r \end{bmatrix} \tag{2.23}$$

Expanding equation (2.23), we get

$$\begin{bmatrix} L \\ M \\ N \end{bmatrix} = \begin{bmatrix} I_{xx}\dot{p} & -I_{xy}\dot{q} & -I_{xz}\dot{r} \\ -I_{xy}\dot{p} & I_{yy}\dot{q} & -I_{yz}\dot{r} \\ -I_{xz}\dot{p} & -I_{yz}\dot{q} & -I_{zz}\dot{r} \end{bmatrix} + \vec{w} \times \begin{bmatrix} pI_{xx} - qI_{xy} - rI_{xz} \\ -pI_{xy} + qI_{yy} - rI_{yz} \\ -pI_{zx} - qI_{zy} + rI_{zz} \end{bmatrix} \tag{2.24}$$

On further simplification of equation (2.24), we get equation (2.25)

$$\begin{bmatrix} L \\ M \\ N \end{bmatrix} = \begin{bmatrix} I_{xx}\dot{p} - I_{xy}\dot{q} - I_{xz}\dot{r} + q(-pI_{xz} - qI_{yz} + rI_{zz}) - r(-pI_{xy} + qI_{yy} - rI_{yz}) \\ -I_{xy}\dot{p} + I_{yy}\dot{q} - I_{yz}\dot{r} - p(-pI_{xz} - qI_{yz} + rI_{zz}) + r(pI_{xx} - qIxy - rIxz) \\ -I_{xz}\dot{p} - I_{yz}\dot{q} - I_{zz}\dot{r} + p(-pI_{xy} + qI_{yy} - rI_{yz}) - q(pI_{xx} - qI_{xy} - rI_{xz}) \end{bmatrix} \tag{2.25}$$

Since in our case, the rigid body is symmetric in the xz and xy plane, the products of inertia tensor are zero and we get the following result.

$$\begin{bmatrix} L \\ M \\ N \end{bmatrix} = \begin{bmatrix} I_{xx}\dot{p} - I_{xz}\dot{r} - qpI_{xz} + qrI_{zz} - rqI_{yy} \\ I_{yy}\dot{q} + p^2I_{xz} - prI_{zz} + rpI_{xx} - r^2Ixz) \\ -I_{xz}\dot{p} + I_{zz}\dot{r} + pqI_{yy} - qpI_{xx} - qrI_{xz} \end{bmatrix} \tag{2.26}$$

The equations of motion are currently in the body-fixed frame. We know that any two coordinate systems can be related through a sequence of three rotations namely the roll, pitch and yaw rotation. The roll ($R_1(\phi)$), pitch($R_2(\theta)$) and yaw($R_3(\psi)$) rotations are defined by (2.27),(2.28) and (2.29).

$$R_1(\phi) = \begin{bmatrix} 1 & 0 & 0 \\ 0 & cos(\phi) & -sin(\phi) \\ 0 & sin(\phi) & cos(\phi) \end{bmatrix} \tag{2.27}$$

$$R_2(\theta) = \begin{bmatrix} cos(\theta) & 0 & sin(\theta) \\ 0 & 1 & 0 \\ -sin(\theta) & 0 & cos(\theta) \end{bmatrix} \tag{2.28}$$

$$R_3(\psi) = \begin{bmatrix} cos(\psi) & -sin(\psi) & 0 \\ sin(\psi) & cos(\psi) & 0 \\ 0 & 0 & 1 \end{bmatrix} \tag{2.29}$$

In our case the p, q, r angular rotations about the body frame are to be converted to euler angular rates about the inertial frame. The angular rotations about the body frame and the angular rates about the inertial frame can be related by (2.30).

$$\vec{V_{BF}} = R_1(\phi)R_2(\theta)R_3(\psi)\vec{V_I} \tag{2.30}$$

The composite rotation matrix about the three rotations is defined by (2.31).

$$R_1(\phi)R_2(\theta)R_3(\psi) = \begin{bmatrix} 1 & 0 & 0 \\ 0 & cos(\phi) & -sin(\phi) \\ 0 & sin(\phi) & cos(\phi) \end{bmatrix} \begin{bmatrix} cos(\theta) & 0 & sin(\theta) \\ 0 & 1 & 0 \\ -sin(\theta) & 0 & cos(\theta) \end{bmatrix} \begin{bmatrix} cos(\psi) & -sin(\psi) & 0 \\ sin(\psi) & cos(\psi) & 0 \\ 0 & 0 & 1 \end{bmatrix} \tag{2.31}$$

This relation will translate the angular rotation vector in the inertial frame to the body-fixed frame. The rate of rotation of the euler angles can be found by rotating the rotation vector to the inertial frame and is shown in (2.32).

$$\begin{bmatrix} p \\ q \\ r \end{bmatrix} = \begin{bmatrix} 1 & 0 & -sin(\theta) \\ 0 & cos(\phi) & cos(\theta)sin(\phi) \\ 0 & -sin(\theta) & cos(\theta)cos(\phi) \end{bmatrix} \tag{2.32}$$

The acceleration vector of the system can be obtained by taking the derivative of the angular rate vector and is shown in (2.33).

$$\begin{bmatrix} \dot{p} \\ \dot{q} \\ \dot{r} \end{bmatrix} = \begin{bmatrix} \ddot{\psi} - cos(\theta)\dot{\theta}\dot{\phi} - sin(\theta)\ddot{\phi} \\ -sin(\psi)\dot{\psi}\dot{\theta} + cos(\psi)\ddot{\theta} + sin\theta\dot{\theta}sin\psi\dot{\phi} - cos\theta cos\psi\dot{\psi}\dot{\phi} - cos\theta sin\psi\ddot{\phi} \\ -cos(\dot{\theta}^2) - sin\theta\ddot{\theta} - sin\theta\dot{\theta}cos\psi\dot{\phi} - cos\theta sin\psi\dot{\psi}\dot{\phi} + cos\theta cos\psi\ddot{\phi} \end{bmatrix} \quad (2.33)$$

The $\dot{p}$, $\dot{q}$, $\dot{r}$ from the above equations are substituted in (2.26) to get the differential rotational equations of motion. The rotational equations of motion tell us about the effect of torque on the rotational dynamics of the system and are shown in (2.34), (2.35) and (2.36).

$$L = I_{xx}\Big(\ddot{\psi} - (cos\theta\dot{\theta}\dot{\phi}) - (sin\theta\ddot{\phi})\Big) + (I_{zz} - I_{yy})\Big((cos(\dot{\psi})\dot{\theta}) - (cos(\theta)sin(\psi)\dot{\phi})\Big)$$
$$\Big((-sin(\theta)\dot{\theta}) + (cos(\theta)cos(\psi)\dot{\phi})\Big) \quad (2.34)$$

$$M = I_{yy}\Big((-sin(\psi)\dot{\psi}\dot{\theta}) + (cos(\psi)\ddot{\theta}) + (sin(\theta)\dot{\theta}sin(\psi)\dot{\phi}) - (cos(\theta)cos(\psi)\dot{\psi}\dot{\phi})$$
$$-(cos(\theta)sin(\psi)\ddot{\phi})\Big) - (I_{zz} - I_{xx})\Big(\big(\dot{\psi} - (sin(\theta)\dot{\phi})\big)\big((-sin(\theta)\dot{\theta}) + (cos(\theta)cos(\psi)\dot{\phi})\big)\Big) \quad (2.35)$$

$$N = I_{zz}\Big(\big(-cos(\theta)(\dot{\theta})^2\big) - \big(sin(\theta)\ddot{\theta} - (sin(\theta)\dot{\theta}cos(\psi)\dot{\phi})\big) - \big(cos(\theta)sin(\psi)\dot{\psi}\dot{\phi}\big)$$
$$+(cos(\theta)cos(\psi)\ddot{\phi})\Big) + (I_{yy} - I_{xx})\Big(\big(\dot{\psi} - (sin(\theta)\dot{\phi})\big)\big((cos(\psi)\dot{\theta}) - (cos(\theta)sin(\psi)\dot{\phi})\big)\Big) \quad (2.36)$$

From equations (2.34),(2.35) and (2.36) the variables $\ddot{\phi}$, $\ddot{\theta}$, $\ddot{\psi}$ can be determined from the linear equation analysis in MATLAB.

2.4 Motor Dynamics

A brush-less dc motor is a type of dc motor which has a high reliability, high efficiency and a high power to volume ratio. The brush-less dc motors are electronically commutated i.e the motor phase currents are changed at appropriate times to produce

the corresponding rotational torque. The BLDC motor is a high performance motor that is capable of producing large amounts of torque over a vast speed range. There are two important parts in the BLDC motor namely the stator windings and the rotor windings. There are two kinds of BLDC motor designs namely the inner and outer rotor design. In an inner rotor design, the stator windings surround the rotor and are attached to the motor's housing. They have the ability to dissipate heat easily and have a greater torque producing capability. The design also has a lower rotor inertia compared with the outer rotor design for easy rotation. In an outer rotor design, the windings are located in the core of the motor and the rotor magnets. The rotor magnets act as an insulator reducing the rate of heat dissipation from the motor and hence, they operate at lower duty cycles or at a lower rated current. Thus, they have the capability only to operate at lower speeds but they provide a low cogging torque.

An electric motor develops torque by alternating the polarity of rotating magnets attached to the rotor and the stationary magnets on the stator surrounding the rotor. The magnets in the stator and rotor can be an electro-magnet or a permanent magnet. Every time, the rotor is rotated by 180 degrees, the position of the north and south poles are reversed to create torque in one direction to account for the reversal of the torque.

Equivalence of a Direct Current Motor: A DC Motor can be approximated as a R-L circuit with voltage applied as input and the emf of the motor as output as shown in Figure 2.3. Using a voltage loop we can say that, the input voltage(V) applied is equal to the voltage drop across the coil resistance(R) and the inductor(L) with the back-emf(E) produced by the motor during rotation.

$$V = IR + L\frac{dI}{dt} + E \tag{2.34}$$

. Let us discuss the effect of voltage and torque on speed during the steady state

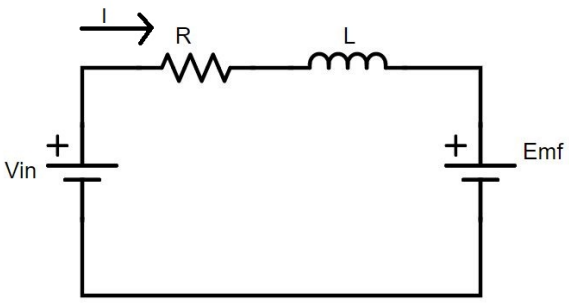

Figure 2.3: Equivalence of the Direct Current Motor

behavior. Since the current flow is constant, the rate of change of inductor current is zero. Since the speed is constant, the torque produced by the motor and the torque produced by the load will be equal. The torque produced by the motor is given by (2.35).

$$T = K_T \phi I \tag{2.35}$$

where K_T represents the torque constant, ϕ is the total flux and T is the load torque.

$$V = \frac{T}{K_T \phi} R + E \tag{2.36}$$

The emf generated by the motor is dependent upon the total flux (ϕ) of the motor and the speed of rotation of the motor(n) which is shown in (2.37).

$$E = K_E \phi n \tag{2.37}$$

Using this value for E, we get the relation between speed and the input voltage applied from (2.38).

$$V = \frac{T}{K_T \phi} R + K_E \phi n \tag{2.38}$$

The equations discussed until now, represent a linear motor, and we transform them to an angular motor assuming the flux to be constant at its peak value. By considering the operation of the motor at maximum flux, the torque constants and electric

constants of the motor are k_t and k_e respectively. The linear speed n is replaced with angular velocity ω. The rotational equations of motion is shown in (2.39).

$$V = \frac{T}{k_t}R + k_e\omega \tag{2.39}$$

The angular velocity can be computed as shown in (2.40).

$$\omega = V - \left(\frac{\frac{T}{k_t}R}{k_e}\right) \tag{2.40}$$

We observe from the equations of motion that the speed of the motor increases with increase in applied voltage. For a fixed applied input voltage, the speed of the motor is inversely affected by the load. The increase in load torque causes reduction in speed of the motor.

2.5 Slipstream Velocity Profile

The rotation of the propellers generates a stream of air underneath them which generates the aerodynamic force for the various torques acting on the system. The slipstream air generated by the propellers depends on the V_∞ velocity of the body. When the body is not in motion, then V_s can be computed with V_∞ to be zero based on the formula shown in (2.41).

$$V_s = \sqrt{\frac{2T_p}{\rho A_p}} \tag{2.41}$$

where T_p is the thrust generated by the propeller, ρ is the density of the medium(air), A_p is the cross-sectional area of the propeller.

When the body is in motion, V_∞ is a numerical value and V_s can be calculated by the formula given in (2.42),(2.43) and (2.44).

$$F_{net} = T_p - (mg) \tag{2.42}$$

where F_{net} is the net force acting on the body, T_p is the thrust generated by the propeller, m is the mass of the drone, g is the acceleration due to gravity.

$$a = \frac{F_{net}}{m} \tag{2.43}$$

where a is the acceleration force acting on the body.

From the linear equations of motion, we know that $v = u + (a \times t)$; where v is the final velocity of the body, u is the initial velocity of the body, t is the duration of the F_{net} force.

The slipstream velocity can now be calculated as shown in (2.44).

$$V_s = \sqrt{\frac{2T_p}{\rho A_p V_\infty^2 + 1}} \tag{2.44}$$

where V_s is the slipstream velocity, T_p is the thrust, A_p is the cross-sectional area of the propeller, V_∞ is the velocity of the body.

2.6 Thrust Profile

The rotation of the propellers powered by a brush-less dc motor converts the rotational energy in to thrust force. The thrust generated by the propellers powers the drone during the vertical and horizontal flight of the drone. When the propellers are rotating, a pressure difference is produced between the forward and rear surfaces of the airfoil shaped propeller blades and the fluid (air) in our case is accelerated behind the propeller. The acceleration behind the propeller leads to an opposite effect in the propeller according to Newtons third law of motion generating the thrust force. The thrust generated by the propeller can be computed by the formula in (2.45).

$$T_p = \frac{C_t \rho d_p^4 w_p^2}{4 \times 3.14^2} \tag{2.45}$$

where C_t is the static thrust coefficient, ρ is the density of the fluid , d_p is the diameter of the propeller, w_p is the rotational speed of the propeller.
The static thrust coefficient is determined based on the geometry of the propeller and for most of the propellers it is 0.1.

2.7 Control Inputs

The control inputs acting on the system are the yawing torque, pitching torque and the rolling torque. The yawing torque(τ_r) is generated by the extension of the rudders in the same direction. The magnitude of yawing torque acting on the system depends on the aerodynamic force(F_r), surface area of the rudder control surfaces (S_r), extension angle of the control surface(θ) and the distance of separation between the center of mass of the system and the center of mass of the control surface in the path of the slipstream air.

$$\tau_r = \vec{F_r} \times \vec{d_r} sin\theta \tag{2.46}$$

where τ_r is the yawing torque, $\vec{F_r}$ is the aerodynamic force, $\vec{d_r}$ is the distance between the center of mass of the system and the rudder control surface, θ is the extension angle of the control surface.
The aerodynamic force (F_r) acting on the control surface is given by

$$\vec{F_r} = \frac{\rho v_s^2 S_r}{2} \tag{2.47}$$

where $\vec{F_r}$ is the aerodynamic force, ρ is the density of the fluid(air), v_s is the slipstream velocity, S_r is the surface area of the rudder in the path of slipstream air flow.

Similarly, the pitching torque(τ_a) is generated by the extension of the ailerons in the same direction. The magnitude of pitching torque acting on the system depends on

the aerodynamic force(F_r), surface area of the aileron control surface(S_a), extension angle of the control surface(θ) and the distance of separation between the center of mass of the system and the center of mass of the control surface in the path of the slipstream air (d_a).

$$\tau_a = \vec{F_a} \times \vec{d_a} sin\theta \tag{2.48}$$

where $\vec{F_a}$ is the aerodynamic force, $\vec{d_a}$ is the distance between the center of mass of the system and the center of mass of the control surface, θ is the extension angle of the control surface.

The aerodynamic force acting on the control surface is given by (2.49).

$$\vec{F_a} = \frac{\rho v_s^2 S_a}{2} \tag{2.49}$$

where $\vec{F_a}$ is the aerodynamic force, ρ is the density of the fluid(air),v_s is the slipstream velocity, S_a is the surface area of the aileron in the path of slipstream air flow.

The extension of the ailerons in opposite direction from each other generates a rolling torque(τ_{roll}) which rotates the drone about its body. The magnitude of rolling torque(τ_{roll}) acting on the system depends on the aerodynamic force (F_{roll}), surface area(S_a), extension angle of the control surface(θ_a) and the distance of separation between the center of mass of the system and the center of mass of the control surface in the path of the slipstream air(d_{roll}).

$$\tau_{roll} = \vec{F_{roll}} \times \vec{d_{roll}} sin(\theta_a) \tag{2.50}$$

where $\vec{F_{roll}}$ is the aerodynamic force, $\vec{d_{roll}}$ is the distance between the center of mass of the system and the center of mass of the control surface, θ is the extension angle of the control surface. The aerodynamic force acting on the control surface is given by (2.51).

$$\vec{F_{roll}} = \frac{\rho v_s^2 S_a}{2} \tag{2.51}$$

where $\vec{F_{roll}}$ is the aerodynamic force, ρ is the density of the fluid (air), v_s is the slipstream velocity, S_a is the surface area of the aileron in the path of slipstream air flow.

Chapter 3

LINEARIZATION

3.1 Introduction

In this chapter, the concept of linearization of a non-linear model is elaborated. The discussion begins by the introduction of linearization of a function and then proceeds with the application of linearization in systems engineering. The application of mathematical ideas for the linearization of a nonlinear function is elaborated. Then the equations of linearization with hover flying as the operating point is explained. In the later half of the chapter, the linearized equations of motion about the different operating points in hover to horizontal transition mode is explained. Then the emphasis moves towards stating the linearized equations of motion about the horizontal flying mode of the drone. Finally the linearized equations of motion about the different operating points in horizontal to hover transition mode is discussed.

3.2 Linearization

Linearization is a technique which computes the linear approximation of a function at a given operating point. Consider a function f(x,y) defined in x $\in (0, \infty)$, $y \in (0, \infty)$. The linearization of the function f(x,y) at a point (a,b) is defined as shown in (3.1).

$$f(x,y) \approx f(a,b) + \frac{\partial f(x,y)}{\partial x}\Big|_{a,b}(x-a) + \frac{\partial f(x,y)}{\partial y}\Big|_{a,b}(y-b) \tag{3.1}$$

Consider a nonlinear dynamic system in matrix form as shown in (3.2).

$$\dot{X(t)} = F(x(t), f(t)), x(t_0) \tag{3.2}$$

where x(t), f(t) and F are respectively the n-dimensional system state space vector, the r-dimensional input vector, and the n-dimensional vector function. Let us consider that $x_n(t)$ is the nominal system trajectory. On performing a taylor series expansion of the system, we get

$$x(t) = x_n(t) + \Delta x(t) \tag{3.3}$$

$$f(t) = f_n(t) + \Delta f(t) \tag{3.4}$$

$$\frac{d}{dt}x_n(t) = \mathcal{F}(x_n(t), f_n(t)) \tag{3.5}$$

From equations (3.3),(3.4),(3.5) and expanding the right-hand side as a taylor series we get,

$$\frac{d}{dt}x_n + \frac{d}{dt}\Delta x = \mathcal{F}(x_n + \Delta x, f_n + \Delta f) \tag{3.6}$$

$$\frac{d}{dt}x_n + \frac{d}{dt}\Delta x = \mathcal{F}(x_n, f_n) + \frac{\partial \mathcal{F}}{\partial x}\bigg|_{f_n(t)}^{x_n(t)} \Delta x + \frac{\partial \mathcal{F}}{\partial f}\bigg|_{f_n(t)}^{x_n(t)} \Delta f + \text{H.O.T} \tag{3.7}$$

Since δx and δf are small values, and these squares are even smaller, the higher order terms are neglected and we get,

$$\frac{d}{dt}\Delta x(t) = \left(\frac{\partial \mathcal{F}}{\partial x}\right)\bigg|_{f_n(t)}^{x_n(t)} \Delta x(t) + \frac{d}{dt}\Delta x(t) = \left(\frac{\partial \mathcal{F}}{\partial f}\right)\bigg|_{f_n(t)}^{x_n(t)} \Delta f(t) \tag{3.8}$$

where,

$$\left(\frac{\partial \mathcal{F}}{\partial x}\right)\bigg|_{f_n(t)}^{x_n(t)} = A^{(n\times n)} = \begin{bmatrix} \frac{\partial \mathcal{F}_1}{\partial x_1} & \frac{\partial \mathcal{F}_1}{\partial x_2} & \cdots & \cdots & \frac{\partial \mathcal{F}_1}{\partial x_n} \\ \frac{\partial \mathcal{F}_2}{\partial x_1} & \frac{\partial \mathcal{F}_2}{\partial x_2} & \cdots & \cdots & \frac{\partial \mathcal{F}_2}{\partial x_n} \\ \vdots & \vdots & \vdots & \vdots & \vdots \\ \frac{\partial \mathcal{F}_n}{\partial x_1} & \frac{\partial \mathcal{F}_n}{\partial x_2} & \cdots & \cdots & \frac{\partial \mathcal{F}_n}{\partial x_n} \end{bmatrix}\Bigg|_{f_n(t)}^{x_n(t)} \tag{3.9}$$

$$\left(\frac{\partial \mathcal{F}}{\partial f}\right)\Big|_{f_n(t)}^{x_n(t)} = B^{(n\times r)} = \begin{bmatrix} \frac{\partial \mathcal{F}_1}{\partial f_1} & \frac{\partial \mathcal{F}_1}{\partial f_2} & \cdots & \cdots & \frac{\partial \mathcal{F}_1}{\partial f_r} \\ \frac{\partial \mathcal{F}_2}{\partial f_1} & \frac{\partial \mathcal{F}_2}{\partial f_2} & \cdots & \cdots & \frac{\partial \mathcal{F}_2}{\partial f_r} \\ \vdots & \vdots & \vdots & \vdots & \vdots \\ \frac{\partial \mathcal{F}_n}{\partial f_1} & \frac{\partial \mathcal{F}_n}{\partial f_2} & \cdots & \cdots & \frac{\partial \mathcal{F}_n}{\partial f_r} \end{bmatrix}\Bigg|_{f_n(t)}^{x_n(t)} \tag{3.10}$$

The jacobian matrices in (3.9) and (3.10) are evaluated at nominal points ($x_{n(t)}$ and $f_{n(t)}$). The resulting linearized system has the form in (3.11).

$$\frac{d}{dt}\Delta x(t) = A\Delta x(t) + B\Delta u(t), \Delta x(t_0) = x(t_0) - x_n(t_0) \tag{3.11}$$

The output differential equations of the given system can be written as $y(t) = \mathcal{G}(x(t), f(t))$. The above equation can be linearized by expanding in a taylor series about nominal points $x_n(t)$ and $f_n(t)$. This results in (3.12).

$$y_n + \Delta y = \mathcal{G}(x_n, f_n) + \left(\frac{\partial \mathcal{G}}{\partial x}\right)\Big|_{f_n(t)}^{x_n(t)}\Delta x + \left(\frac{\partial \mathcal{G}}{\partial f}\right)\Big|_{f_n(t)}^{x_n(t)}\Delta f + \text{H.O.T} \tag{3.12}$$

By neglecting the higher order terms and simplifying the above expression yields (3.13).

$$\Delta y = \left(\frac{\partial \mathcal{G}}{\partial x}\right)\Big|_{f_n(t)}^{x_n(t)}\Delta x + \left(\frac{\partial \mathcal{G}}{\partial f}\right)\Big|_{f_n(t)}^{x_n(t)}\Delta f \tag{3.13}$$

where,

$$\Delta y(t) = C\Delta x(t) + D\Delta f(t)$$

$$C^{(p\times n)} = \left(\frac{\partial \mathcal{G}}{\partial x}\right)\Big|_{f_n(t)}^{x_n(t)} = \begin{bmatrix} \frac{\partial \mathcal{G}_1}{\partial x_1} & \frac{\partial \mathcal{G}_1}{\partial x_2} & \cdots & \cdots & \frac{\partial \mathcal{G}_1}{\partial x_n} \\ \frac{\partial \mathcal{G}_2}{\partial x_1} & \frac{\partial \mathcal{G}_2}{\partial x_2} & \cdots & \cdots & \frac{\partial \mathcal{G}_2}{\partial x_n} \\ \vdots & \vdots & \frac{\partial \mathcal{G}_i}{\partial x_j} & \vdots & \vdots \\ \frac{\partial \mathcal{G}_n}{\partial x_1} & \frac{\partial \mathcal{G}_n}{\partial x_2} & \cdots & \cdots & \frac{\partial \mathcal{G}_n}{\partial x_n} \end{bmatrix}\Bigg|_{f_n(t)}^{x_n(t)} \tag{3.14}$$

$$D^{(p\times r)} = \left(\frac{\partial \mathcal{G}}{\partial f}\right)\Big|_{f_n(t)}^{x_n(t)} = \begin{bmatrix} \frac{\partial \mathcal{G}_1}{\partial f_1} & \frac{\partial \mathcal{G}_1}{\partial f_2} & \cdots & \cdots & \frac{\partial \mathcal{G}_1}{\partial f_n} \\ \frac{\partial \mathcal{G}_2}{\partial f_1} & \frac{\partial \mathcal{G}_2}{\partial f_2} & \cdots & \cdots & \frac{\partial \mathcal{G}_2}{\partial f_n} \\ \vdots & \vdots & \frac{\partial \mathcal{G}_i}{\partial f_j} & \vdots & \vdots \\ \frac{\partial \mathcal{G}_n}{\partial f_1} & \frac{\partial \mathcal{G}_n}{\partial f_2} & \cdots & \cdots & \frac{\partial \mathcal{G}_n}{\partial f_n} \end{bmatrix}\Bigg|_{f_n(t)}^{x_n(t)} \tag{3.15}$$

Linearization reduces the complexity of the non-linear system and the linearized version behaves exactly the same way as the non-linear one at the linearized operating point. As we move away from the operating point we would observe the differences between the linearized and non-linear model. The magnitude in the differences between the two systems depend on the non-linearities present in the system.

3.3 Linearized Model of the Drone

The linearization technique derived in the previous section can be applied about a particular operating point of the system. For our plane, we would want to compute the linearized model about the hover flying mode, different operating points in the hover to horizontal flying mode, horizontal flying mode and the different operating points in horizontal to hover flying mode. We choose the number of operating points in the hover to horizontal transition flight and the horizontal to hover transition flight depending on the degree of closeness we would like the nonlinear system to behave with respect to the linear system. The values of the states of the system namely the yaw angle, yaw angular rate, pitch angle, pitch angular rate, roll angle, roll angular rate and the inputs namely the yawing torque, pitching torque and the rolling torque are utilized and the linearized Jacobian matrices can be computed. From the linearized jacobian matrices, the linearized model can be computed using

the formula shown in (3.16).

$$A = \begin{bmatrix} \frac{\partial f_1}{\partial x_1} & \frac{\partial f_1}{\partial x_2} & \cdots & \cdots & \frac{\partial f_1}{\partial x_6} \\ \frac{\partial f_2}{\partial x_1} & \frac{\partial f_2}{\partial x_2} & \cdots & \cdots & \frac{\partial f_2}{\partial x_6} \\ \vdots & \vdots & \vdots & \vdots & \vdots \\ \frac{\partial f_6}{\partial x_1} & \frac{\partial f_6}{\partial x_2} & \cdots & \cdots & \frac{\partial f_6}{\partial x_6} \end{bmatrix}_{x=x1_{o1},x2_{o1},x3_{o1},x4_{o1},x5o1,x6_{o1}}$$

$$B = \begin{bmatrix} \frac{\partial f_1}{\partial u_1} & \frac{\partial f_1}{\partial u_2} & \frac{\partial f_1}{\partial u_3} \\ \frac{\partial f_2}{\partial u_1} & \frac{\partial f_2}{\partial u_2} & \frac{\partial f_2}{\partial u_3} \\ \vdots & \vdots & \vdots \\ \frac{\partial f_6}{\partial u_1} & \frac{\partial f_6}{\partial u_2} & \frac{\partial f_6}{\partial u_3} \end{bmatrix}_{u=u1_{o1},u2_{o1},u3_{o1}}$$

$$C = \begin{bmatrix} \frac{\partial g_1}{\partial x_1} & \frac{\partial g_1}{\partial x_2} & \cdots & \cdots & \frac{\partial g_1}{\partial x_6} \\ \frac{\partial g_2}{\partial x_1} & \frac{\partial g_2}{\partial x_2} & \cdots & \cdots & \frac{\partial g_2}{\partial x_6} \\ \frac{\partial g_3}{\partial x_1} & \frac{\partial g_3}{\partial x_2} & \cdots & \cdots & \frac{\partial g_3}{\partial x_6} \end{bmatrix}_{x=x1_{o1},x2_{o1},x3_{o1},x4_{o1},x5o1,x6_{o1}}$$

$$D = \begin{bmatrix} \frac{\partial g_1}{\partial u_1} & \frac{\partial g_1}{\partial u_2} & \frac{\partial g_1}{\partial u_3} \\ \frac{\partial g_2}{\partial u_1} & \frac{\partial g_2}{\partial u_2} & \frac{\partial g_2}{\partial u_3} \\ \frac{\partial g_3}{\partial u_1} & \frac{\partial g_3}{\partial u_2} & \frac{\partial g_3}{\partial u_3} \end{bmatrix}_{u=u1_{o1},u2_{o1},u3_{o1}}$$

$$Tf = C(sI - A^{-1})B + D \tag{3.16}$$

Chapter 4

CONTROLLER DESIGN

4.1 Introduction

In this chapter, we study about the controller design techniques from [6], [10], [44]. The infinity norm of signals and systems is explained at the beginning. Then the PID loop shaping controller design is discussed where the K_p, K_i, K_d parameters are optimized to match the selected target loop. Then the linear quadratic regulator design is explained which solves the matrix riccati equations to arrive at a controller guaranteeing robustness properties. Finally, the H_∞ loop shaping control technique is explained where the loop shapes for the sensitivity, complementary sensitivity are selected and the algorithm generates an optimal design minimizing the H_∞ norm of the desired function.

Infinity Norm of Signals and Systems :

For a signal x(t), the infinity norm is given by:

$$||x(t)||_\infty = \sup ||x(t)|| \tag{4.1}$$

For a system defined by a transfer function G(s), the H_∞ norm of a stable system is

$$||G||_\infty = \max_w |G(jw)| \tag{4.2}$$

The infinity norm of a system can also be said as the peak of the Bode magnitude plot of the system. For a multi-variable system, the SISO gain $|G(jw)|$ at a given frequency should be generalized to the multi-variable case. For an n $\times$ m transfer function matrix $G(s)$, the method to achieve this is to introduce the maximum gain

of $G(jw)$ at the frequency w. For this reason, we introduce the euclidean norm $||v||$ of a complex- valued vector $v = [v_1 \cdots v_m] \in C_m$ which is given by,

$$||v|| = (|v_1|^2 + \cdots |v_m|^2)^{1/2} \tag{4.3}$$

The peak magnitude of G at the frequency w is given by the formula in (4.4).

$$||G(jw)|| = \max_v \left\{ \frac{G(jw)v}{||v||} : v \neq 0, v \in C_m \right\} \tag{4.4}$$

$$||G(jw)|| = \max_v \left\{ ||G(jw)v|| : ||v|| = 1, v \in C^m \right\} \tag{4.5}$$

The matrix norm $||G(jw)||$ is equal to the maximum singular value $\sigma(G(jw))$ of the matrix $G(jw)$. Hence the H_∞ norm can be expressed as shown in (4.6).

$$||G||_\infty = sup_w(G(jw)) \tag{4.6}$$

4.2 PID Loop Shaping Control Design

In this chapter, the controller design technique by the PID loop shaping tuning technique is presented. PID control technique is the simplest way of control system design to stabilize and automate any system. The PID controller has the proportional, integral and the derivative component in its structure. The proportional term produces an output value proportional to the current error value. The proportional term contributes $K_p e(t)$ to the controller output. The integral term contributes an action proportional to the magnitude of the error and the duration of the error. The integral term contributes $K_i \int_0^t e(\tau)d\tau$ to the controller output. The derivative term contributes an output that is proportional to the slope of the error over time and it contributes $K_d \frac{de(t)}{dt}$.

The derivative action predicts system behavior improving settling time and the stability of the system. An ideal derivative action is not causal and so an additional low pass filtering for the derivative term is required to have a bi-proper transfer function. The tuning of a control loop can be done by multiple techniques namely ziegler- nichols tuning, cohen-coon method and the relay method. Although the controller tuning can be performed based on the methods shown above, an optimal method to tune the PID controller is by a method namely PID tuning by frequency loop shaping which is explained in [46]. In this technique, the controller parameters are adjusted for the plant (P) that makes the open loop gain PC close to the loop shape L obtained from LQR, in the sense of minimizing the H_∞ norm. The equation of a PID control law is shown in (4.7).

$$u(t) = C(s)[r(t) - y(t)] = \left[k_p + \frac{k_i}{s} + \frac{k_d s}{\tau s + 1}\right][r(t) - y(t)] \tag{4.7}$$

The controller can be written in terms of a bi-proper transfer function as shown in (4.8).

$$C(s) = k_1 s^2 + k_2 s + \frac{k_3}{s(\tau s + 1)} \tag{4.8}$$

where $k_1 = k_d + k_p\tau$, $k_2 = k_i\tau + k_p$, $k_3 = k_i$.

The controller tuning can be performed based on the parameters k_1, k_2, k_3 and hence the parameters k_p, k_i, k_d can be computed. The PID control optimization is easy to work and we can formulate a convex optimization problem to choose the controller parameters k_1, k_2, k_3 which minimizes the following norm.

$$\min_{k_1,k_2,k_3} ||W_1(GC_{k_1,k_2,k_3} - L)||_\infty \tag{4.9}$$

The Weighting function (W_1) is selected as shown in (4.10)

$$||W_1(jw)|| \geq \left|\frac{1}{1+L(jw)}\right|, \forall w \tag{4.10}$$

The above equation satisfies the robust stability criterion as indicated by the small gain theorem which is stated in (4.11).

$$||S_0\Delta||_\infty = \left|\frac{1}{1+L}(GC-L)\right|_\infty \leq 1 \tag{4.11}$$

The equation (4.11) states the small gain theorem statement for the divisive uncertainty. The target loop for the open loop optimization is chosen based on the stability condition of the plant. For a plant having unstable poles, the target loop selection would generally provide a better guess in the sense of stability. For a plant with stable poles and not having any slow poles, the target loop can be chosen as $L = \frac{\lambda}{s}$. And, for a stable plant having slow poles, the target loop is chosen as $L = \frac{\lambda(s+a)}{s(s+\epsilon)}$. Since the PID controller has limited degrees of freedom, it is necessary to augment the controller with low pass filters to provide adequate roll off at high frequencies for noise attenuation.

4.3 LQR Control Design

Linear quadratic regulator is a quadratic optimization method subject to a dynamic system constraint producing a full state feedback control system design with desired stability and robustness. A cost function is minimized to generate a desired control output. Consider a system of the form shown in (4.12).

$$\dot{X} = Ax + Bu, x(0) = x_0 \tag{4.12}$$

An optimization problem is formulated that has a state feedback control law u = -kx which drives the initial condition to zero. Consider the quadratic cost function shown

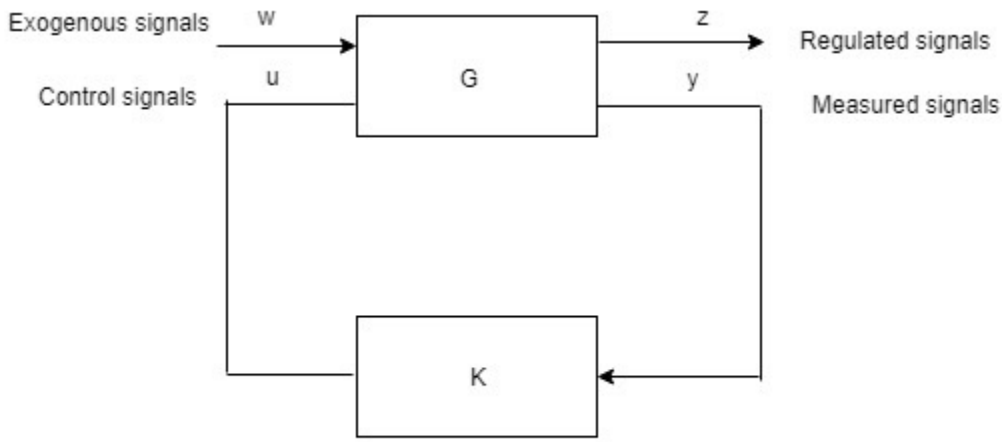

Figure 4.1: Block Diagram of Standard H_∞ Control Loop

in (4.13).

$$J = \int_0^\infty [x^T(t)Qx(t) + u^T T(t)Ru(t)]dt \tag{4.13}$$

By applying the algorithms from (4.12) and (4.13), and minimizing the cost function, the control law can be formulated as:

$$u = -Kx = R^{-1}B^T P\times \tag{4.14}$$

where P is the solution to the control algebraic riccati equation.

$$A^T P + PA - PBR^{-1}B^T P + Q = 0 \tag{4.15}$$

The system is guaranteed to be robust and stable if Q and R are positive definite.

4.4 H_∞ Loop Shaping Control Design

H_∞ control technique is a method in which design specifications are given in the sense of H_∞ norm of the system guaranteeing robustness and sensitivity reduction. Consider the standard H_∞ system block diagram as shown in Figure 4.1.

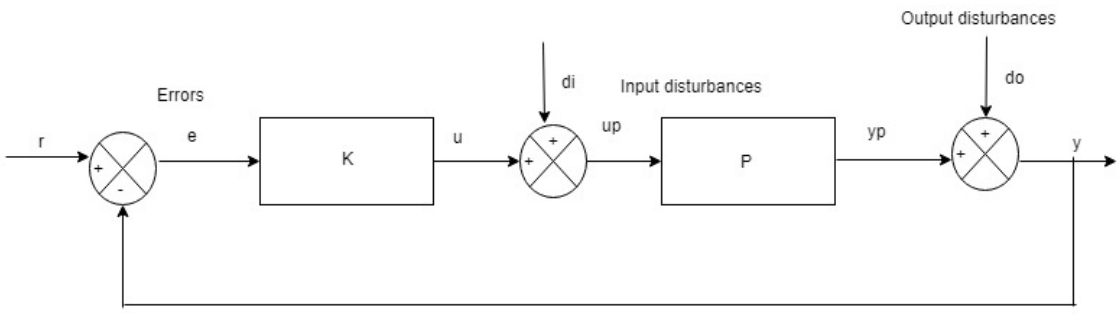

Figure 4.2: Closed Loop Feedback Control System

The objective of the H_∞ design technique is to make the H_∞ norm of the closed loop transfer function T_{wz} smaller than a chosen performance metric $\gamma > 0$. The exogenous signals (w) include reference commands to the control system, disturbances acting on the system and sensor noise. The signal u represents the control signals or manipulated variables. The regulated signals (z) include tracking errors, actuator/ control outputs and signal estimation errors. The measured signals (y) include measurements or signals that are directly available to the controller K. The measured signals include the plant state variables, measurable plant outputs, measurable control signals and measurable exogenous signals. There are two kinds of H_∞ control techniques namely optimal H_∞ control and standard H_∞ control. In optimal H_∞ control, the problem is defined to minimize the H_∞ norm of the system and in standard H_∞ control, the H_∞ norm of the system is made under a certain level. A controller K is obtained from the technique that internally stabilizes the system G such that the H_∞ norm of the closed loop system transfer function matrix T_{wz} is minimized.

$$\min_K ||T_{wz}||_{H_\infty} \tag{4.16}$$

The system in the Figure (4.2) can be transformed to the standard H_∞ control loop. The inputs to the plant are the reference signal(w) and the control output

signal(u). The outputs of the system are the error signal (z) and the plant output (y). The relation between (w, z) and (u, y) is given by (4.17).

$$\begin{bmatrix} u \\ y \end{bmatrix} = \begin{bmatrix} P_{11}(s) & P_{12}(s) \\ P_{21}(s) & P_{22}(s) \end{bmatrix} \begin{bmatrix} w \\ z \end{bmatrix} \tag{4.17}$$

Now the system can be partitioned as

$$P = \begin{bmatrix} A & B \\ C & D \end{bmatrix}$$

On further partitioning the system for two inputs and two outputs, we get P as

$$\begin{bmatrix} A & B_1 & B_2 \\ C_1 & D_{11} & D_{12} \\ C_2 & D_{12} & D_{22} \end{bmatrix}$$

From this partition, we can express the system in state space as shown in (4.18).

$$\begin{aligned} \dot{x} &= Ax + B_1 w + B_2 z \\ y_1 &= C_1 x + D_{11} w + D_{12} z \\ y_2 &= C_2 X + D_{12} w + D_{22} u_{22} \end{aligned} \tag{4.18}$$

When the system T_{wz} is linear time invariant, we can express T_{wz} as :

$$T_{wz} = P_{11}(s) + P_{12}(s)[I - K(s)P_{22}(s)]^{-1} K(s) P_{21}(s) \tag{4.19}$$

There can also be a special case where the internal stability of the system is guaranteed, and the system is stabilizable and observable, then there exists a minimal entropy controller which is also called the central controller is shown in (4.20).

$$K_\infty = \begin{bmatrix} A_\infty & -Z_\infty L_\infty \\ F_\infty & 0 \end{bmatrix} \tag{4.20}$$

where,

$$A_\infty = A + \gamma^{-2} B_1 B_1^T X + B_2 F_\infty + Z_\infty L_\infty C_2 \tag{4.21}$$

$$F_\infty = -B_2^T X \tag{4.22}$$

$$L_\infty = -Y C_2^T \tag{4.23}$$

$$Z_\infty = (I - \gamma^{-2} Y X)^{-1} \tag{4.24}$$

and $X \geq 0$ is the solution to the control algebraic riccati equation in equation (4.25).

$$A^T X + X A + X(\gamma^{-2} B_1 B_1^T - B_2 B_2^T) X + C_1^T C_1 = 0, X \geq 0 \tag{4.25}$$

$Y \geq 0$ is the solution to the filter algebraic riccati equation in (4.26).

$$Y A^T + A Y + Y(\gamma^{-2} C_1 C_1^T - C_2 C_2^T) X + B_1 B_1^T = 0 \tag{4.26}$$

There is also a technique called weighted H_∞ mixed sensitivity design where the weighting functions are specified for sensitivity, complementary sensitivity, control sensitivity to shape the frequency responses of the corresponding functions. In this design, we define weighting functions to formulate an H_∞ suboptimal control problem to address the desired performance measures of the system.

Figure 4.3 shows a weighting w_1 on the signal y, a weighting function w_2 on the controls u, and a weighting w_3 on the plant outputs. From the figure, we observe that the regulated signals $Z = [z_1 \;\; z_2 \;\; z_3]$ are related to the exogenous signals w as follows:

$Z_1 = W_1 z_1$, $Z_2 = W_2 z_2$, $Z_3 = W_3 z_3$. From this, we can say that the closed loop transfer function matrix (T_{wz}) from w to z is given by (4.27).

$$T_{wz} = \begin{bmatrix} W_1 S \\ W_2 K S \\ W_3 T \end{bmatrix} \tag{4.27}$$

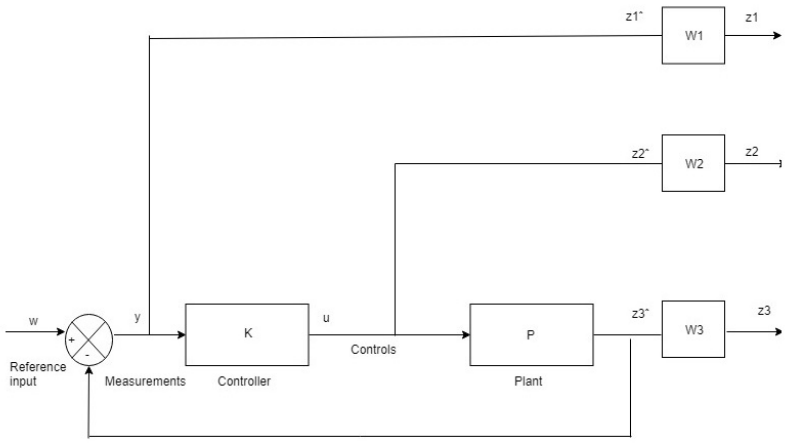

Figure 4.3: Weighted H_∞ Mixed Sensitivity Design

Since, T_{wz} has the various sensitivity transfer function matrices, the problem is called as weighted H_∞ mixed sensitivity problem. The objective of this design is to minimize the transfer function $T_{wz} \leq \gamma$. We also discuss about the selection of weighting functions for the different sensitivities. While designing the weighting function for the sensitivity, we would like to have $||W_1 S||_\infty < \gamma$. From this, it follows that $\sigma_{\max}[S(jw)] \leq W_1^{-1}\gamma$. From this, we select the sensitivity weighting function W_1 on the sensitivity S as:

$$W_1 = \left[\frac{k_1(s+z_1)}{s+p_1}\right] \tag{4.28}$$

where k_1 >0, $z_1 \geq p_1 \geq 0$.

The parameter k_1 is chosen to be a large value. The parameter p_1 is typically selected to be small. These selections make the sensitivity function heavily penalized at low frequencies. The above selection of weighting function W_1 results in (4.29).

$$\sigma_{\max}[S(jw)] \leq |W_1(jw)^{-1}|\gamma \tag{4.29}$$

Similarly, we can select the control weighting W_2 on KS as,

$$W_2 = \left[\frac{k_2(s+z_2)}{s+p_2}\right] \tag{4.30}$$

where $k_2, p_2, z_2 \geq 0$ are chosen so that the resulting KS is not too large. The above selection of W_2 results in $\sigma_{max}[K(jw)S(jw)] \leq |W_2(jw)^{-1}|\gamma$ and KS lies below $|W_2^{-1}\gamma|$. We can select the output weighting W_3 on T as follows:

$$W_3 = \left[\frac{k_3(s+z_3)}{s+p_3}\right], \tag{4.31}$$

$$\text{with } k_3 > 0, p_3 > z_3 > 0 \ .$$

Such a weighting would penalize T more heavily at higher frequencies. Such a selection for W_3 results in $W_3\sigma_{\max}[T(jw)] \leq |W_3(jw)^{-1}|\gamma$ and T lies below $T \leq |W_3^{-1}|\gamma$. When choosing the weighting functions for desired properties, there must be good separation between low and high frequency specifications. The low frequency (command following and disturbance attenuation) specifications on the sensitivity function should be sufficiently separated in frequency range from high frequency (robustness and noise attenuation) specifications imposed on KS and on the complementary sensitivity T. When the low frequency and high frequency specifications overlap, then we would have a problem with the H_∞ suboptimal design and care must be taken to avoid this overlap.

4.5 Experiment Design

In this section, the experimental design to obtain the dynamical model of the motor is discussed. The brush-less DC motor with its contra-rotating propellers is mounted on a wooden plank. An experimental setup with the IR transmitter and IR receiver setup is placed on a setup in such a way that the propeller passes through the path of IR light and blocks the receiver from receiving the infrared light. The IR transmitter and IR receiver setup is placed on a wooden support beam. The IR

transmitter is connected in forward bias with a forward resistance(R_f). While setting up the experiment, precautions must be taken to ensure that the IR light from the transmitter has direct incidence on the receiver. The IR receiver is connected in series with a load resistor of 10 kΩ and the analog output voltage is measured across the load resistor. The analog output voltage across the resistor is given to an ADC pin of the arduino due micro-controller sampled at 2 Khz. The data from the ADC pin is serially transmitted and recorded on a computer.

Chapter 5

SYSTEM DESIGN AND THEORETICAL RESULTS

5.1 Introduction

In this chapter, the VTOL drone we studied in this project is described. Then the results of system modeling by first principles technique is presented. Also, the linearized model of the system about hovering mode, hover to horizontal transition flying, horizontal flying mode, horizontal to hover flying mode are presented. Next, the controller design by H_∞ loop shaping technique is presented. Then, the experimental setup and results for determining the dynamical model of the motor are presented. Then, the results of the slipstream velocity analysis for different speeds of rotation of the motor is presented. Next, the thrust profile for different speeds of rotation of the motor is presented. Finally, the torque acting on the system for a yawing action, pitching action and rolling action for varying speeds of rotation are presented.

5.2 Description of VTOL Drone

The three view drawing of the VTOL drone is shown in Figure 5.1. Figure 5.2 provides a 3D graph of the VTOL drone. The VTOL drone has a cuboidal body shape made of styrofoam in its central location. To this body, wings are attached on its four faces. The wings with larger surface area has the aileron control surfaces on its bottom edge. The wings with smaller surface area has the rudder control surfaces on its bottom edge. The thrust force for take-off is generated by a brush-less dc motor to which the contra-rotating propellers are attached. The wing configuration of the plane is similar to the Lockheed XFV-1. The yaw and pitch rotations are

controlled by the rudder control surfaces and aileron control surfaces respectively. The roll rotation can be controlled by either of the aileron control surfaces or the rudder control surfaces. For the purpose of horizontal flying, the wing surface which houses the ailerons are designed in the shape of an airfoil to provide lift.

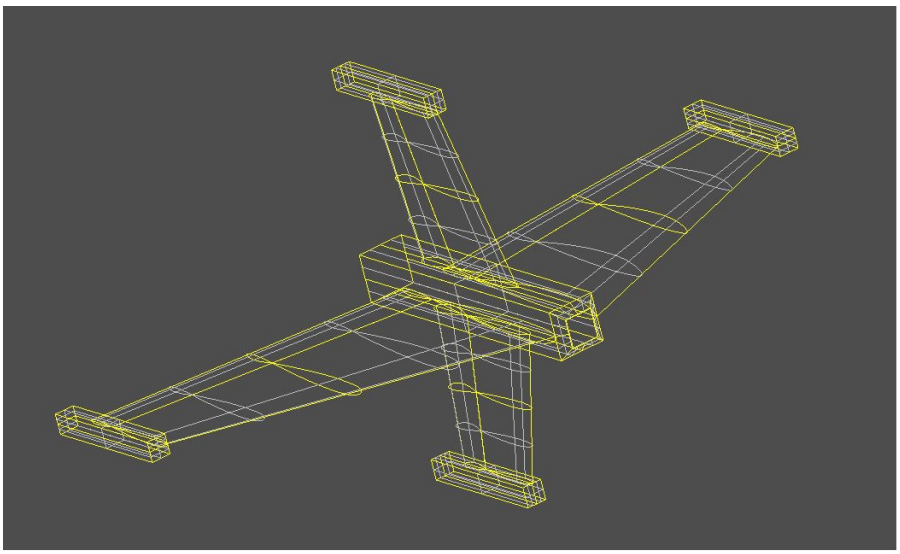

Figure 5.1: 3D Graph of the VTOL Drone

5.3 System Modeling

The modeling of the VTOL drone is done based on first principles modeling. First, the mass distribution of the VTOL drone is analyzed based on the different materials used for building the drone. The center of mass is computed and is determined to be 15.5414 inches from the bottom face of the central cuboid. The moment of inertia tensor of the drone is computed based on adding the moments of inertia of the individual components about the center of mass. For many of the components, the moment of inertia is determined about their own center of mass and then is transformed about the drone's center of mass. The moment of inertia tensor(I) of the drone is computed about the principal x, y, z axis passing through the center of mass

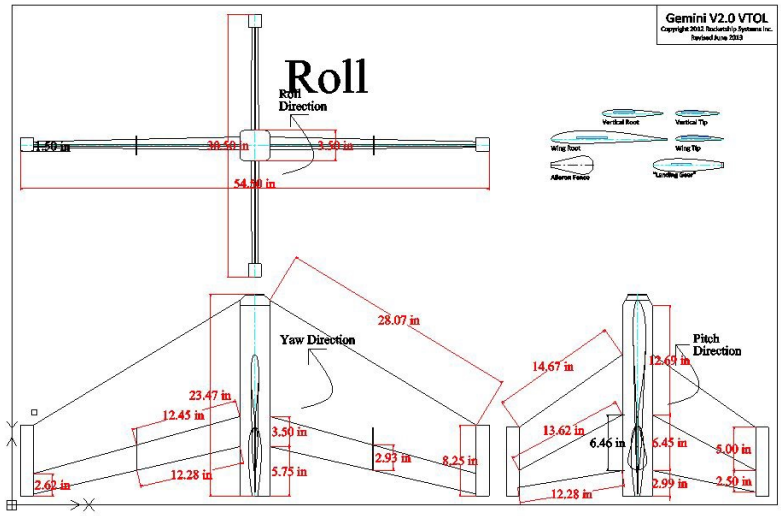

Figure 5.2: Three View Drawing of the VTOL Drone

and is determined to be:

$$I = \begin{bmatrix} 0.2174 & 0 & 0 \\ 0 & 0.0578 & 0 \\ 0 & 0 & 0.1312 \end{bmatrix}$$

The parameters of the drone are utilized in the differential equations of motion to get the non-linear dynamics of the plane about the hovering mode and horizontal flying mode. For representing the system in state-space, the state variables of the system are x_1(yaw angle), x_2 (yaw angular rate), x_3 (pitch angle), x_4 (pitch angular rate), x_5 (roll angle) and x_6(roll angular rate). The control inputs are u_1(yawing torque), u_2(pitching torque), u_3(rolling torque), and with the outputs being y_1(yaw angle), y_2(pitch angle), y_3(roll angle) .

The non-linear equations of motion are linearized about the hover operating mode ($x_1 = 0, x_2 = 0, x_3 = 0, x_4 = 0, x_5 = 0, x_6 = 0, u_1 = 0, u_2 = 0, u_3 = 0$) to get the

linearized equations of motion about the hovering mode which is shown in (5.1).

$$G = \begin{bmatrix} 0 & 0 & \frac{4.6}{s^2} \\ 0 & \frac{17.3}{s^2} & 0 \\ \frac{7.622}{s^2} & 0 & 0 \end{bmatrix} \tag{5.1}$$

Similarly, the differential equations of motion are linearized about horizontal flying mode ($x_1 = 0, x_2 = 0, x_3 = 0, x_4 = 0, x_5 = 0, x_6 = 0, u_1 = 0, u_2 = 0, u_3 = 0$) to get the linearized equations of motion which is shown in (5.2).

$$G = \begin{bmatrix} \frac{7.622}{s^2} & 0 & 0 \\ 0 & \frac{17.27}{s^2} & 0 \\ 0 & 0 & \frac{4.598}{s^2} \end{bmatrix} \tag{5.2}$$

The torques acting on the plane for a yawing action, pitching action and rolling action are modeled according to the distance between the center of mass of the control surface and the center of mass of the drone. The measurements are made for the rudder and aileron control surfaces. The aerodynamic force acting on the control surface and the displacement of the control surface can be modeled to compute the exact torque acting on the system for a yawing action and pitching action.

5.4 Controller Design

The controllers are designed based on H_∞ loop shaping technique. The controller is implemented as an inner-outer loop for the regulation of angular rate and angle dynamics. The inner loop controller regulates the angular rate dynamics and the outer loop controller regulates the angle dynamics. The weighting functions for the sensitivity and the complementary sensitivity of the angular rate dynamics are chosen as shown in (5.3). The controllers stabilizing the dynamics of the system in hover mode are shown in (5.5)-(5.10).

$$W_1 = \frac{1.5(s+0.1)}{(s+10)}$$
$$W_2 = \frac{0.15(s+100)}{(s+10)} \tag{5.3}$$

The weighting functions for the sensitivity and the complementary sensitivity of the angle dynamics are chosen as shown in (5.4).

$$W_1 = \frac{1.5(s+0.1)}{(s+5)}$$
$$W_2 = \frac{0.15(s+50)}{(s+5)} \tag{5.4}$$

The bode plots of the weighting functions of the sensitivity and complementary sensitivity function are shown in Figure 5.3(a), Figure 5.3(b) for the inner and outer loop respectively. The inner and outer loop controllers for the yaw, pitch and roll dynamics are shown in (5.5)-(5.10).

Controller (Yaw Angular Rate) :

$$C_1 = \frac{67.46s^2 + 8.108e^4 s + 393}{s^3 + 276.2s^2 + 3.172e^4 s + 2838} \tag{5.5}$$

Controller (Yaw Angle) :

$$C_{o1} = \frac{4.755s^2 + 9744s - 9.509e^{-14}}{s^3 + 23.61s^2 + 2312s + 322.4} \tag{5.6}$$

Controller (Pitch Angular Rate) :

$$C_2 = \frac{3054s + 5.265e^5}{s^2 + 206.3s + 4.746e^5} \tag{5.7}$$

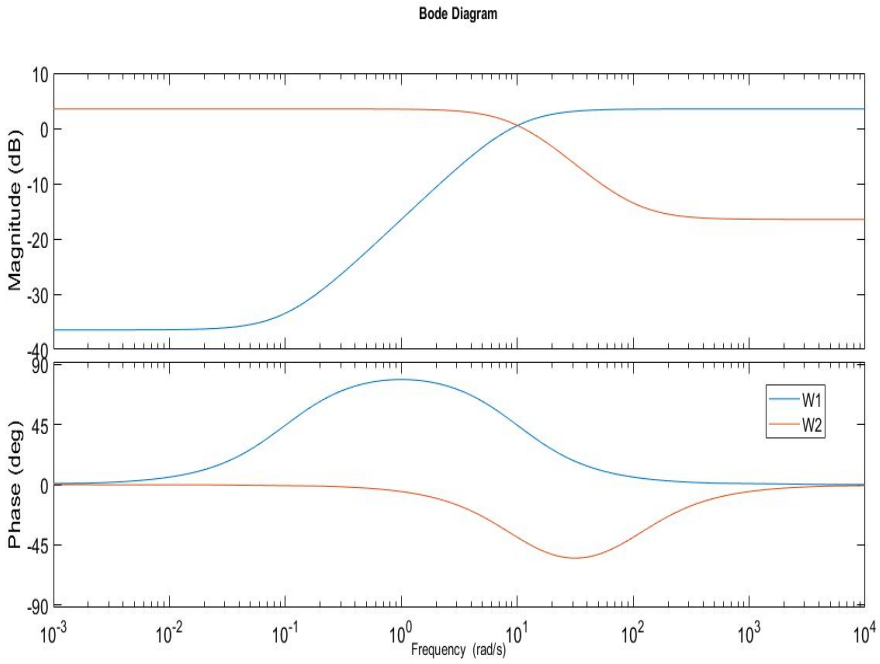

(a) S and T Weighting Functions of the Inner Loop

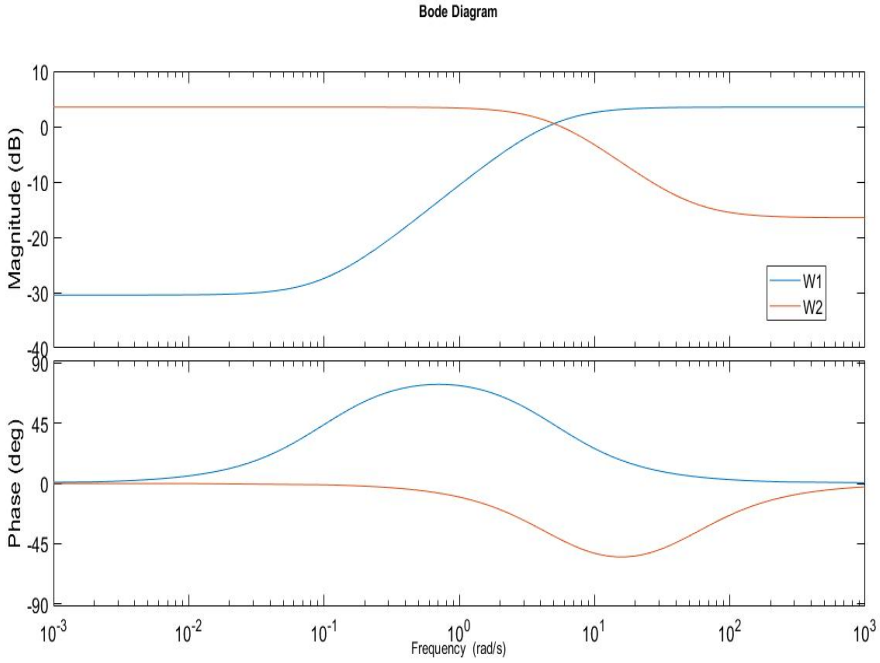

(b) S and T Weighting Functions of the Outer Loop

Figure 5.3: Bode Plots of the S and T Weighting Functions

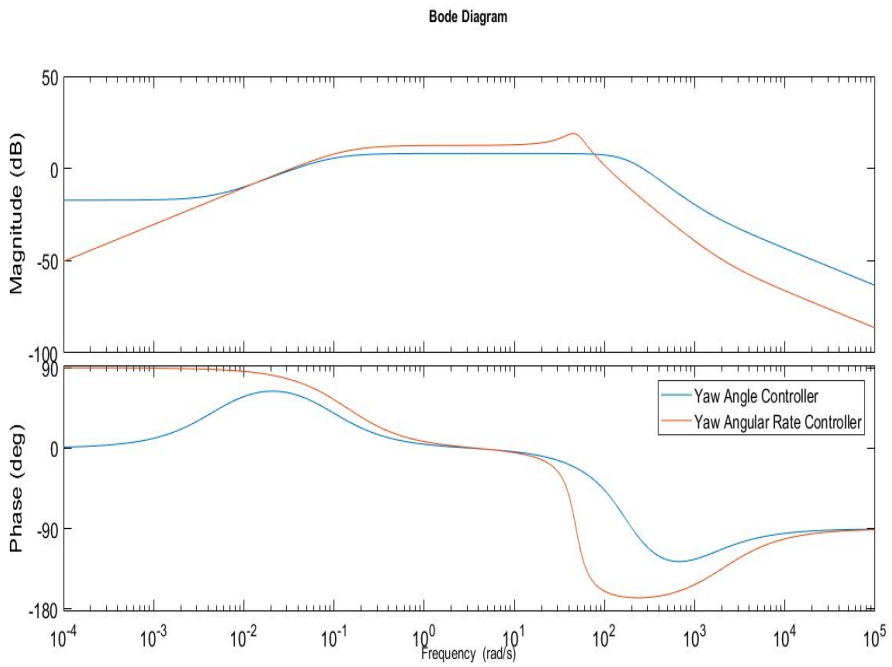

Figure 5.4: Bode Plot of Yaw Controller

Controller (Pitch Angle) :

$$C_{o2} = \frac{4.841s^2 + 1.441e^4 s + 1.86e^{-12}}{s^3 + 32.55s^2 + 3311s + 401.2} \tag{5.8}$$

Controller (Roll Angular Rate) :

$$C_3 = \frac{4.689s^2 + 3804s + 1.236e^{-12}}{s^3 + 41.04s^2 + 1454s + 153.7} \tag{5.9}$$

Controller (Roll Angle) :

$$C_{o3} = \frac{225s^2 + 3.518e^5 s + 4514}{s^3 + 130s^2 + 2.529e^5 s + 2.689e^4} \tag{5.10}$$

The Bode plots of the controllers for the yaw, pitch and roll dynamics are shown in Figure (5.4),(5.5) and (5.6).

The controllers designed for the hover mode will work for the horizontal flying

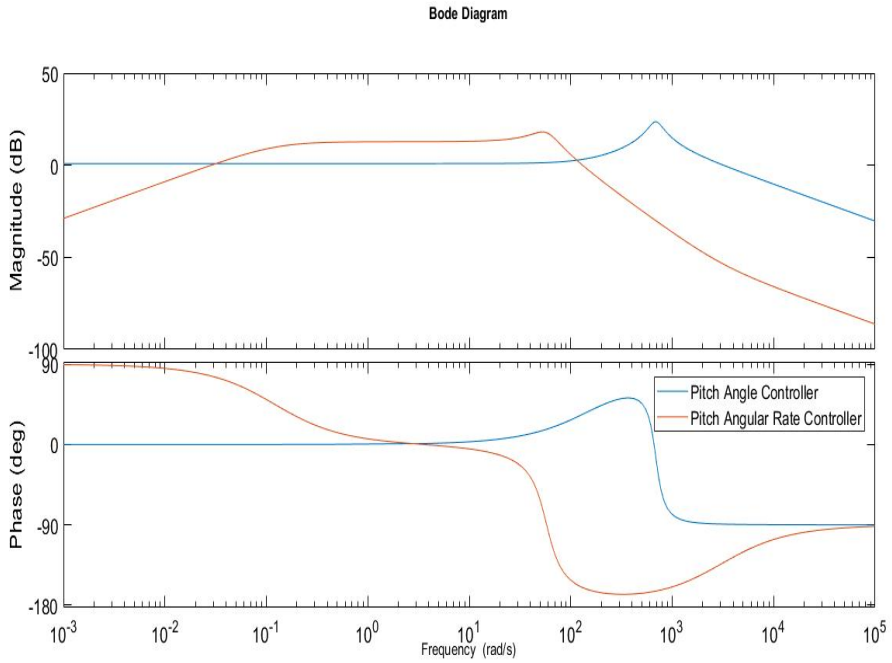

Figure 5.5: Bode Plot of Pitch Controller

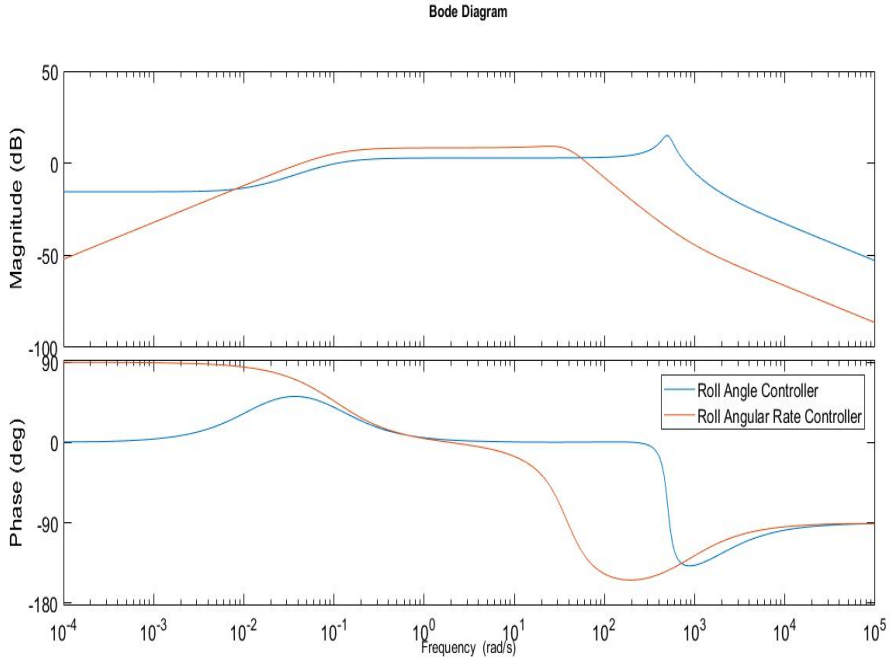

Figure 5.6: Bode Plot of Roll Controller

mode except for the fact that, the rotation about the principal x-axis becomes the roll rotation, and the rotation about the principal z-axis becomes the pitch rotation. The controllers stabilizing the dynamics of the system in the horizontal mode are shown in (5.11)- (5.16).

Controller (Yaw Angular Rate) :

$$C_1 = \frac{4.689s^2 + 3804s + 1.236e^{-12}}{s^3 + 41.04s^2 + 1454s + 153.7} \tag{5.11}$$

Controller (Yaw Angle) :

$$C_{o1} = \frac{225s^2 + 3.518e^5 s + 4514}{s^3 + 130s^2 + 2.529e^5 s + 2.689e^4} \tag{5.12}$$

Controller (Pitch Angular Rate) :

$$C_2 = \frac{3054s + 5.265e^5}{s^2 + 206.3s + 4.746e^5} \tag{5.13}$$

Controller (Pitch Angle) :

$$C_{o2} = \frac{4.841s^2 + 1.441e^4 s + 1.86e^{-12}}{s^3 + 32.55s^2 + 3311s + 401.2} \tag{5.14}$$

Controller (Roll Angular Rate) :

$$C_3 = \frac{67.46s^2 + 8.108e^4 s + 393}{s^3 + 276.2s^2 + 3.172e^4 s + 2838} \tag{5.15}$$

Controller (Roll Angle) :

$$C_{o3} = \frac{4.755s^2 + 9744s - 9.509e^{-14}}{s^3 + 23.61s^2 + 2312s + 322.4} \tag{5.16}$$

The sensitivity and complementary sensitivity bounds of the closed loop system are satisfied for the hover and horizontal mode operating point. The bode plots of the sen-

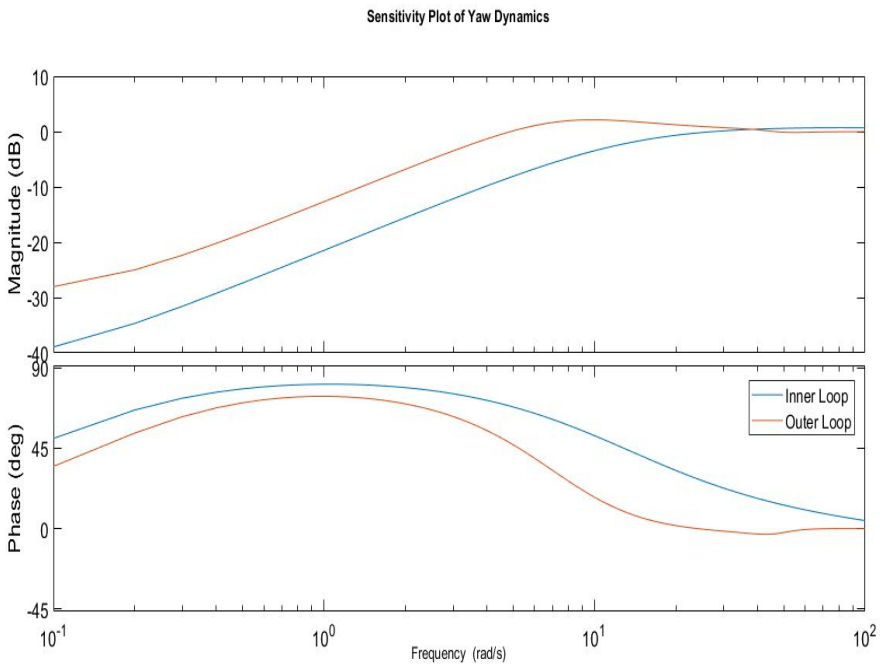

Figure 5.7: Sensitivity Plot of Yaw Dynamics

sitivity and complementary sensitivity functions of the yaw, pitch and roll dynamics are shown in Figure (5.7)-(5.12).

5.5 Motor Dynamical Model

In this section, the dynamical model of the brush-less dc motor is obtained. As shown in section 4.5, the experimental setup is utilized to compute the motor dynamical model. The motor is operated at different inputs to the electronic speed controller which controls the speed of the motor. The data from the IR transmitter-receiver is collected for speed analysis as well to analyze the noise in the measurement. The fast fourier transform of the sensor data is analyzed to determine the noise frequency associated with the sensor measurement and the results are shown in Figure 5.13. After analyzing the spectrum of the noise, a second order low pass filter is designed with a cut-off frequency of 0.1 Hz, 0.01 dB tolerance in peak-peak ripple, 80 dB stopband

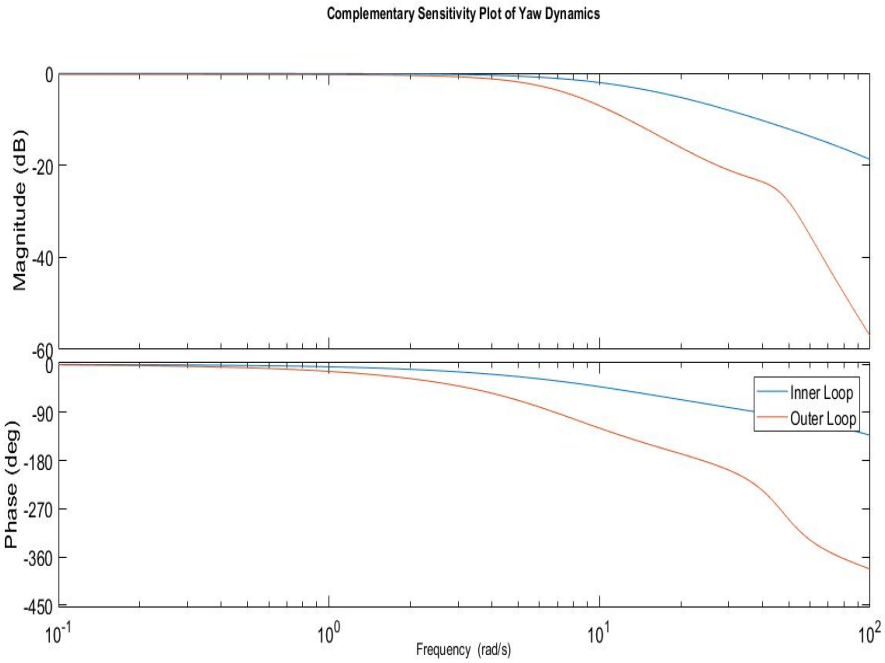

Figure 5.8: Complementary Sensitivity Plot of Yaw Dynamics

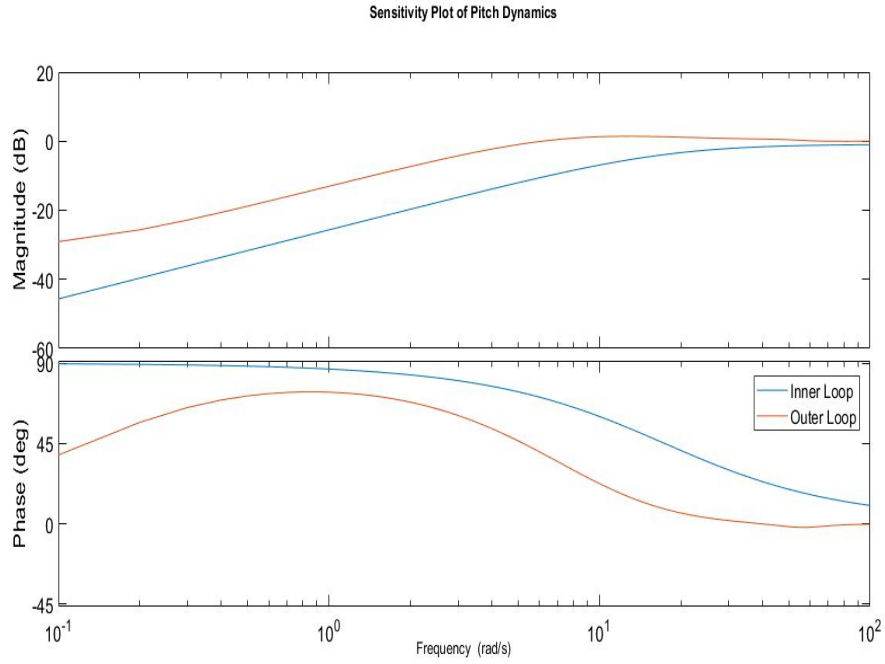

Figure 5.9: Sensitivity Plot of Pitch Dynamics

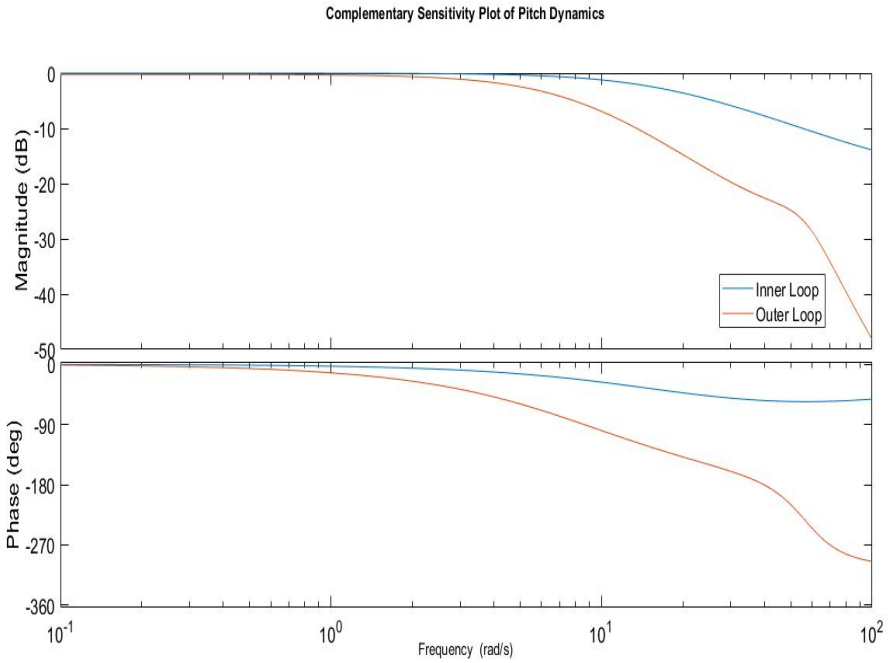

Figure 5.10: Complementary Sensitivity Plot of Pitch Dynamics

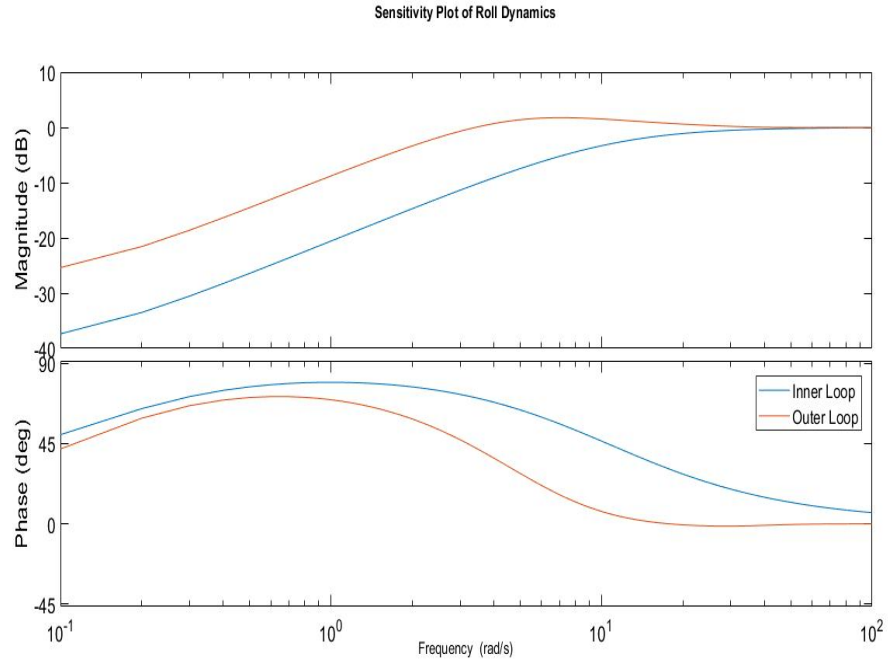

Figure 5.11: Sensitivity Plot of Roll Dynamics

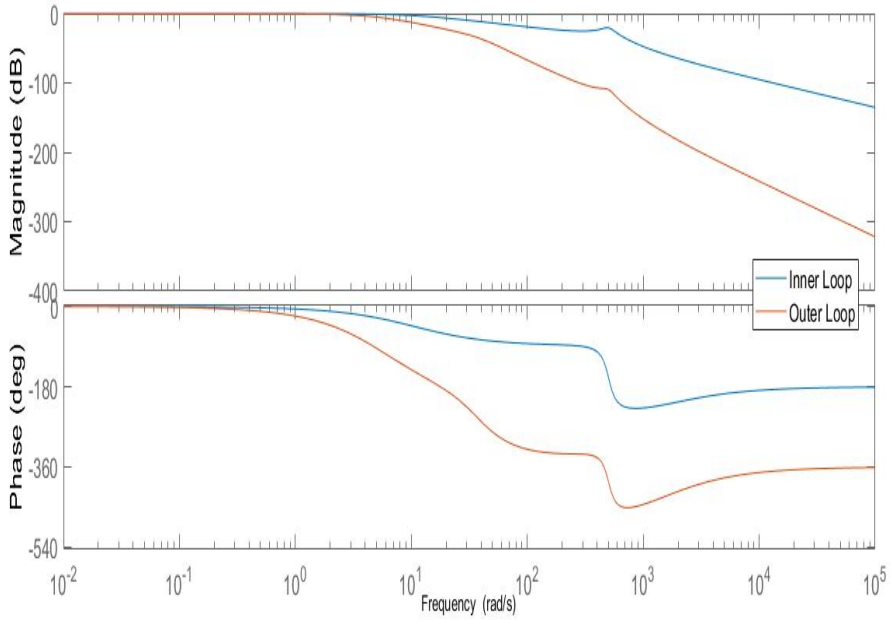

Figure 5.12: Complementary Sensitivity Plot of Roll Dynamics

attenuation and the magnitude plot of the filter is shown in Figure 5.14. The sensor data is filtered and is used for data analysis. Based on the filtered data, the speed of rotation of the motor is determined and the results are plotted in Figure 5.15.

5.6 Slipstream Velocity Analysis

In this section, the velocity of slipstream of air is analyzed for different speeds of rotation of the brush-less dc motor. The slipstream velocity increases at a small rate during lower speeds of rotation from 3000 to 5000 rpm. Then, the slipstream velocity increases at a greater rate from 6000 rpm to 8000 rpm. And after a rotational speed of 8000 rpm, the slipstream velocity has the maximum rate of increase and reaches close to 160 m/sec for a speed of 12000 rpm. The major range of operation of the brush-less dc motor for our application is between 6000 rpm to 10000 rpm and we put a greater emphasis between this operating range. The graph between the slipstream

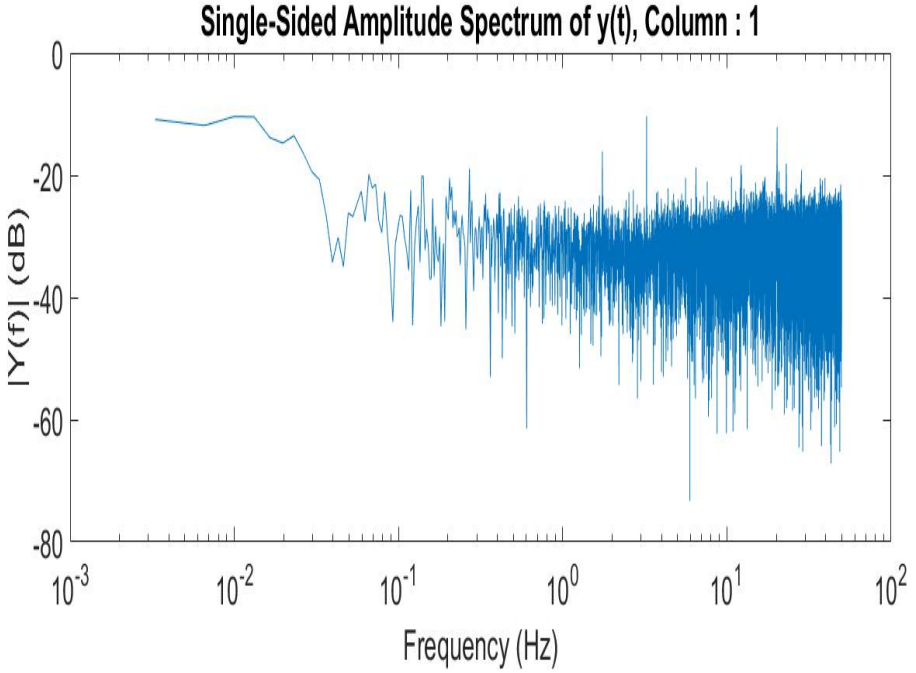

Figure 5.13: Fast Fourier Transform of Noise in Infrared Sensor Measurement

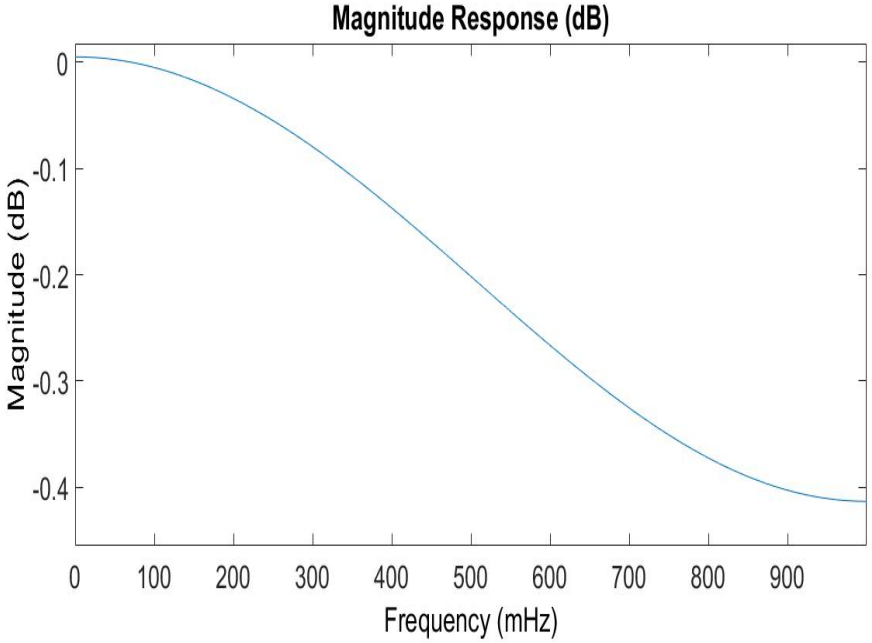

Figure 5.14: Bode Plot of Low Pass Filter

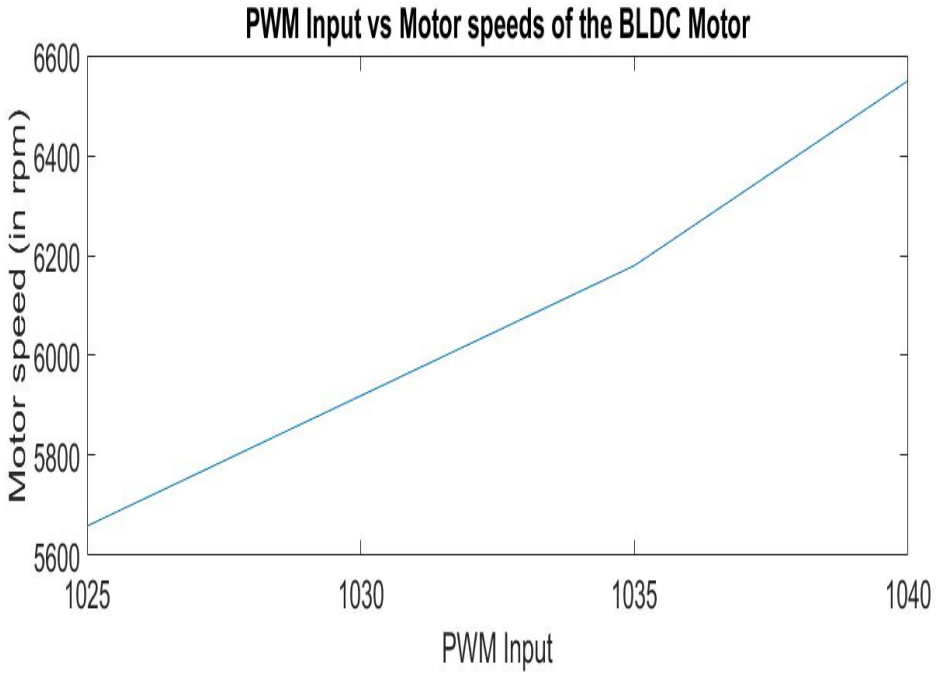

Figure 5.15: Pulse Width Modulated Input Vs Motor Speed

velocity and the speed of rotation of the propellers is shown in Figure 5.16.

5.7 Thrust Profile Analysis

The thrust profile of the drone is analyzed in this section. For the different speeds of rotation of the propeller, the thrust generated by the brush-less dc motor is analyzed for the operation of the drone. The thrust generated reaches close to 20 Newtons for a rotational speed of 6000 rpm. Then it increases in a parabolic rate reaching 80 Newtons for a rotational speed of 12000 rpm. Our emphasis is on an operating range from 6000 to 10000 rpm for which we have the thrust profile clearly available from Figure 5.17.

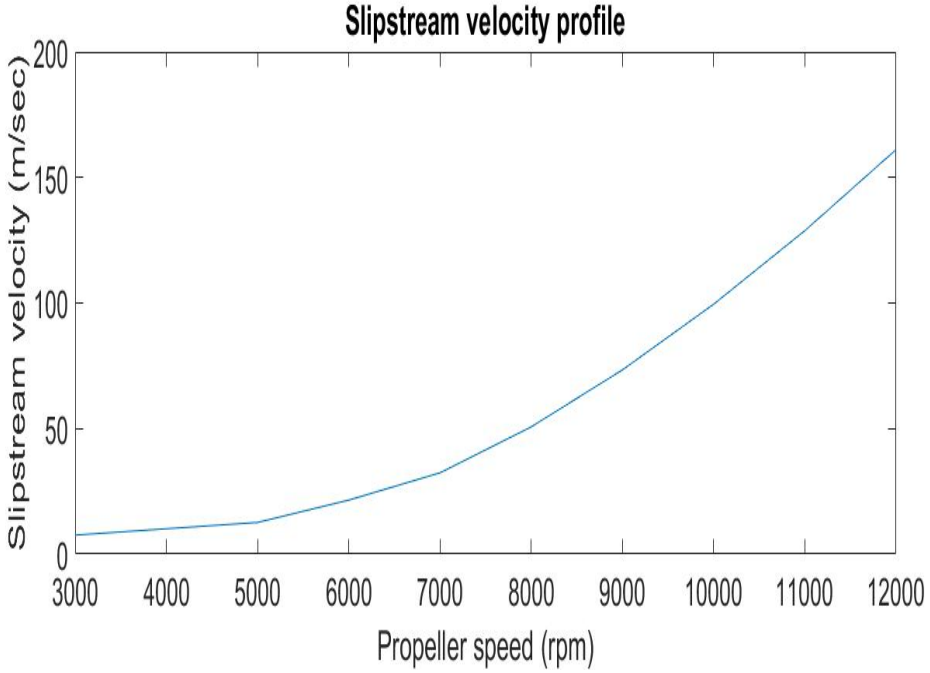

Figure 5.16: Slipstream Velocity Characteristics

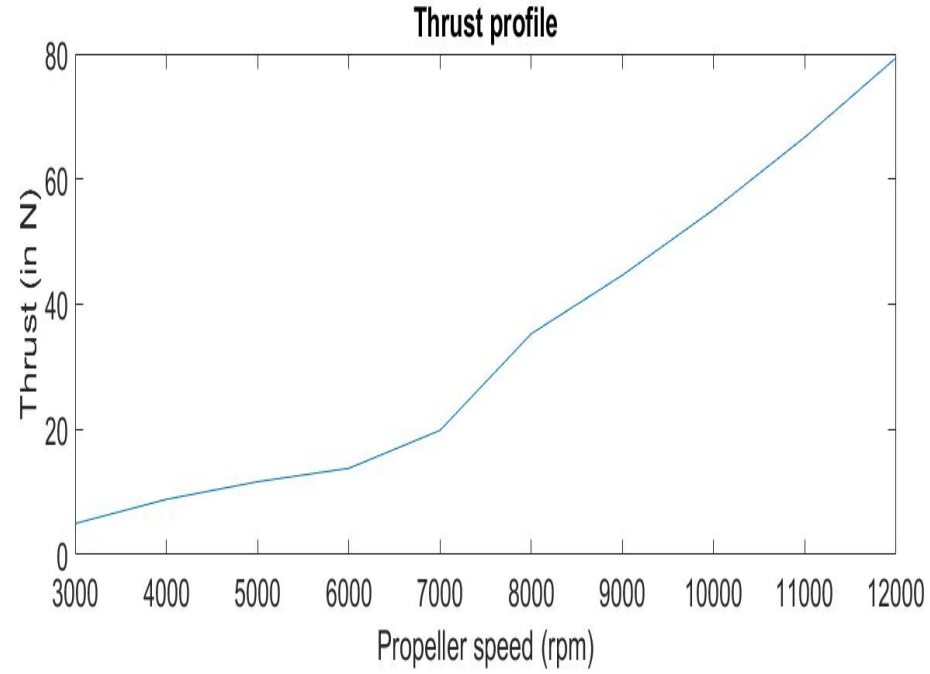

Figure 5.17: Thrust Profile Characteristics

5.8 Torque Profile Analysis

The torque profile of the rudder input and aileron input is analyzed in this section. The characteristics of torque are analyzed for three different speeds of rotation of the brush-less dc motor in 6000 rpm, 8000 rpm and 10000 rpm. Let us discuss the yawing torque acting on the system on the extension of rudder control surfaces. The yawing torque increases by a constant rate(k_{r1}) for a rotational speed of 6000 rpm to a steady increase in flap angle of the control surfaces and reaches 0.5 N-m for a complete extension of the rudders in either direction. For a rotational speed of 8000 rpm, the profile increases by a constant rate (k_{r2}) to a steady increase in flap angle where k_{r2} $>k_{r1}$ and it reaches a yawing torque of 1.9 N-m for the complete extension. When the brush-less dc motor is operated at a rotational speed of 10000 rpm, the yawing torque profile increases by a rate (k_{r3}) to the steady increase in flap angle where k_{r3} $>k_{r2}$ $>k_{r1}$ and reaches a peak of 7.2 N-m. The yawing torque profile for the extension of control surfaces is shown in Figure 5.18. From the pwm input vs torque output analysis for a rudder input, the reverse mapping of the torque input vs pwm output can also be obtained. This relation for a torque input on the rudder control surface is shown in Figure 5.18a. This analysis helps in precise application of torque input by means of a pulse-width modulated signal input to the servos actuating the control surface deflection.

Let us discuss the pitching torque acting on the system due to the deflection of the aileron control surfaces. The pitching torque increases by a constant rate (k_{a1}) to a steady increase in flap angle of the aileron control surfaces for the operation of the brush-less dc motor at a speed of 6000 rpm. The pitching torque reaches a peak value of 0.5 N-m to the complete flap extension. When the motor is operated at a speed of 8000 rpm, the pitching torque steadily increases by a constant rate (k_{a2}) where

$k_{a2} > k_{a1}$ to a steady increase in flap angle of the aileron control surface and reaches a peak value of 1.9 N-m to a complete flap extension in either direction. While operating the motor at a speed of 10000 rpm the pitching torque increases by a constant rate (k_{a3}) where $k_{a3} > k_{a2} > k_{a1}$ and reaches a peak value of 7.4 N-m to a complete flap extension of the aileron control surface. The pitching torque profile for the extension of control surfaces is shown in Figure 5.19. This relation for a torque input on the aileron control surface is shown in Figure 5.19a .

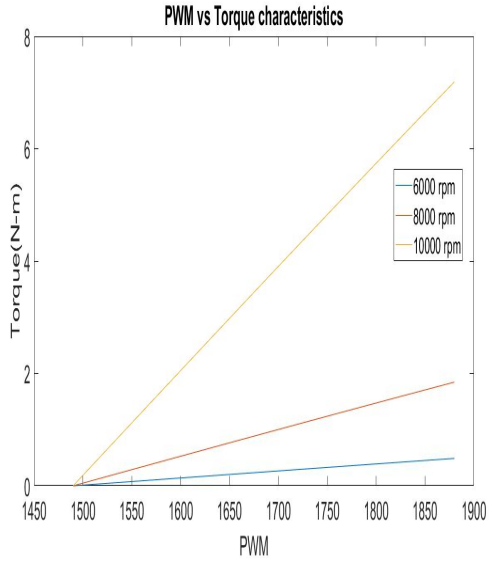

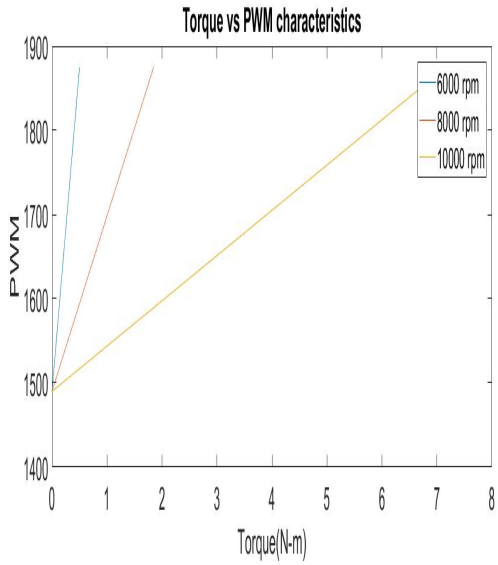

(a)Pwm Input Vs Torque Characteristics (b) Torque Vs Pwm Input Characteristics

Figure 5.18: Characteristics of Rudder Control Surface

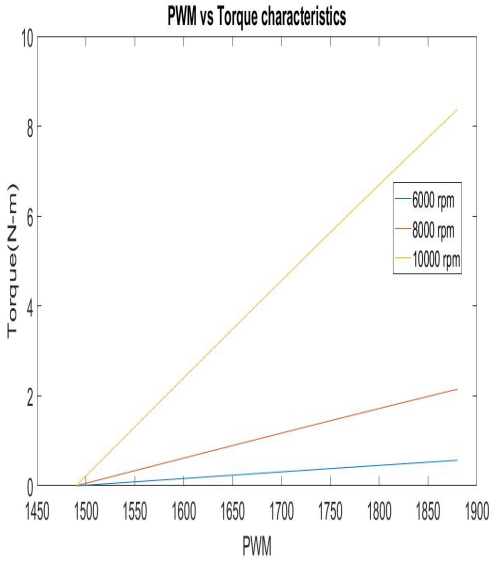

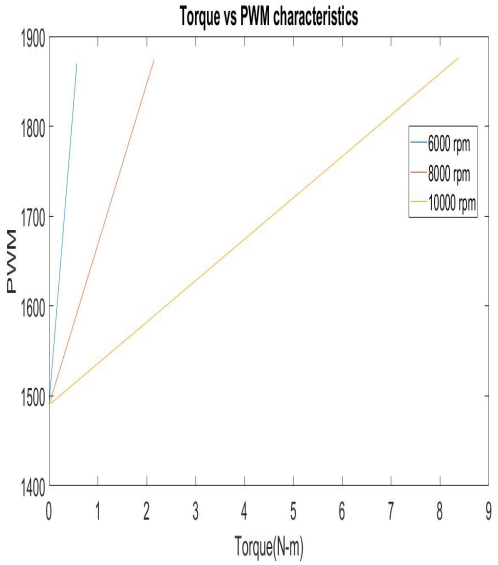

(a)Pwm Input vs Torque Characteristics (b) Torque vs Pwm Input Characteristics

Figure 5.19: Characteristics of Aileron Control Surface

Chapter 6

SIMULATION RESULTS

6.1 Hover Flying Mode

The hover flying of the VTOL drone is simulated in SIMULINK in this section. The controllers designed for the linearized model of the drone about hover flying are tested on the non-linear dynamical model of the drone. The drone is operated at a rotational speed of 9000 rpm. An unit step reference command is tracked by the closed loop yaw control system, closed loop pitch control system and the closed loop roll control system. The step response plots of the angular rate dynamics (yaw, pitch, roll) and the angle dynamics(yaw, pitch, roll) are shown in Figure 6.1.

The reference tracking of the closed loop yaw control system with step changes in reference angle input is shown in Figure 6.2. The reference tracking of the closed loop pitch control system with step changes in angle reference input is shown in Figure 6.3. The reference tracking of the roll control system with step changes in angle reference input is shown in Figure 6.4.

6.2 Hover to Horizontal Flying Transition Mode

The hover to horizontal transition flight of the VTOL drone is simulated in SIMULINK in this section. The controllers designed for the linearized model of the drone about hover flying is tested on the non-linear dynamical model of the drone. The drone is operated at a rotational speed of 9000 rpm from the hover position until the pitch down angle of 38 degrees. Then the motor is operated at a rotational speed of 8500 rpm from the pitch down angle of 38 degrees until 68 degrees of pitch down

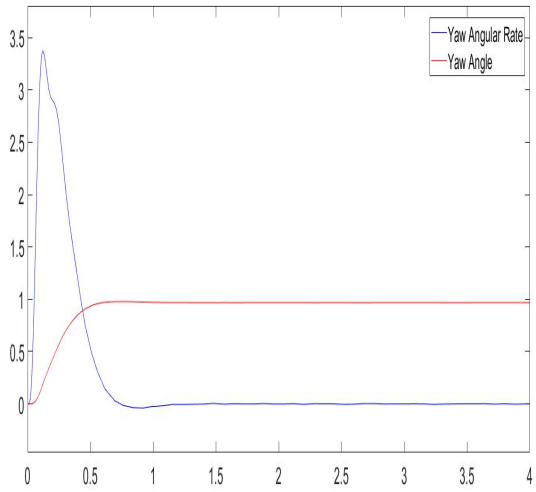

(a) Yaw Dynamics

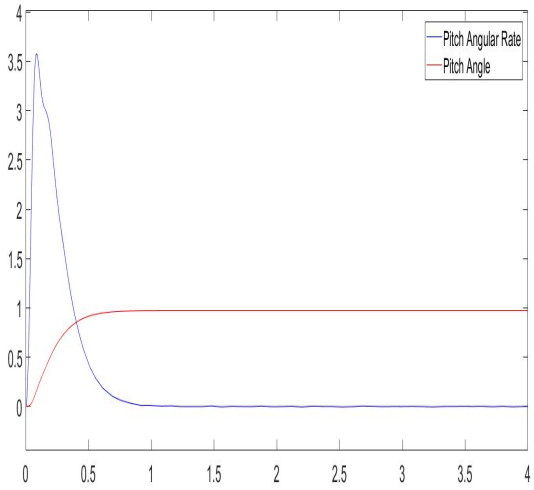

(b) Pitch Dynamics

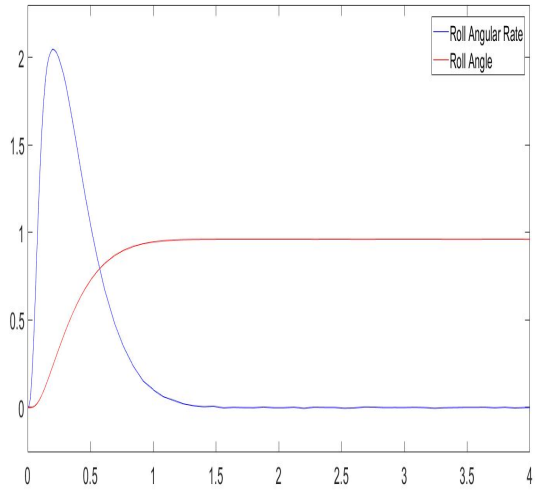

(c) Roll Dynamics

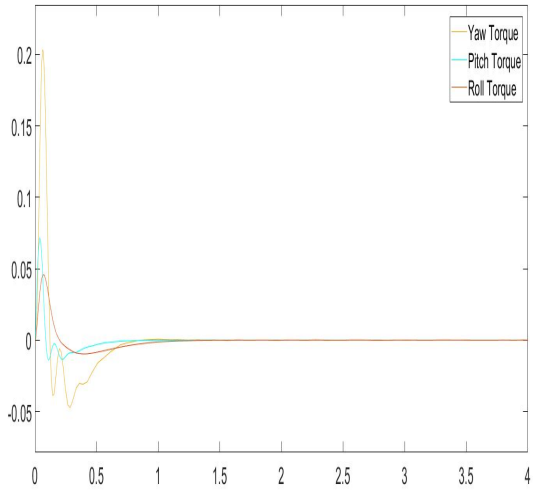

(d) Control Inputs

Figure 6.1: Hover Mode - Closed Loop Reference Tracking

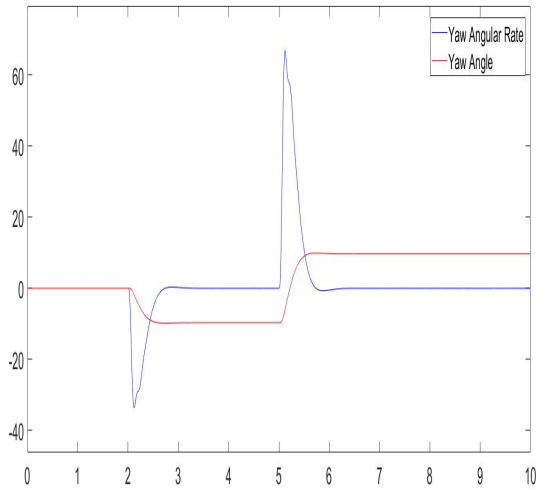

(a) Yaw Dynamics

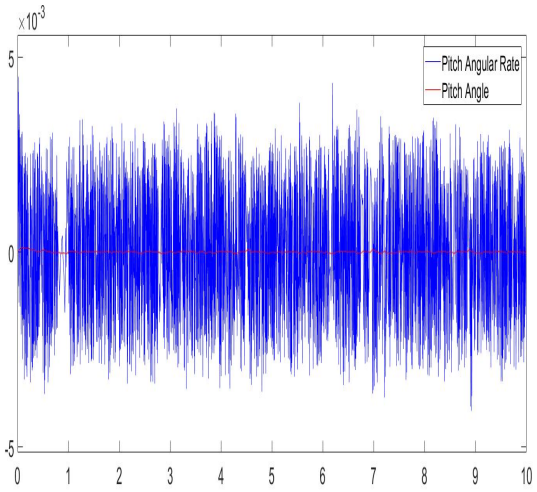

(b) Pitch Dynamics

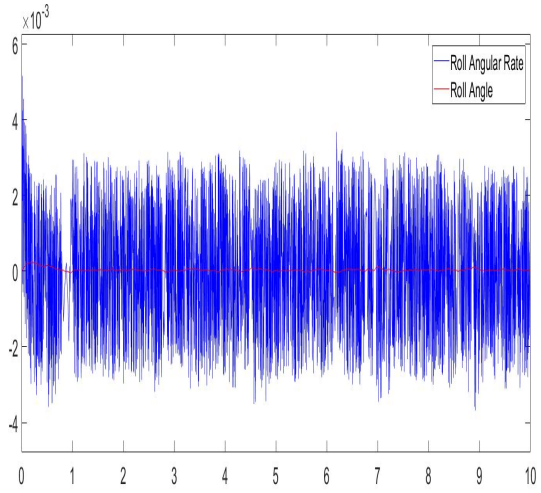

(c) Roll Dynamics

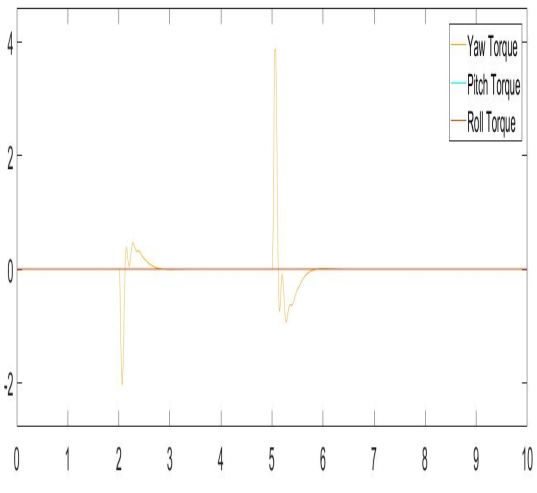

(d) Control Inputs

Figure 6.2: Hover Mode - Yaw Reference Input Tracking

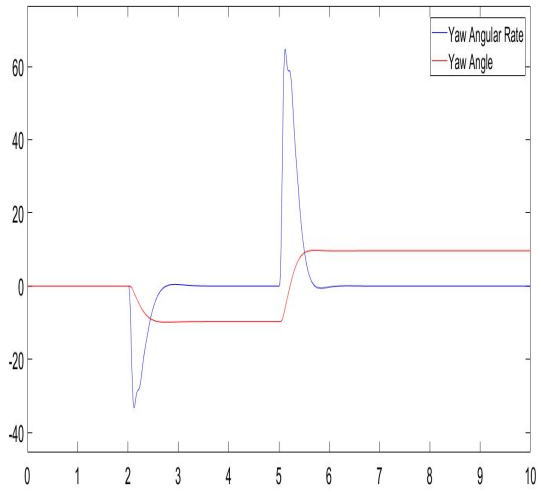

(a) Yaw Dynamics

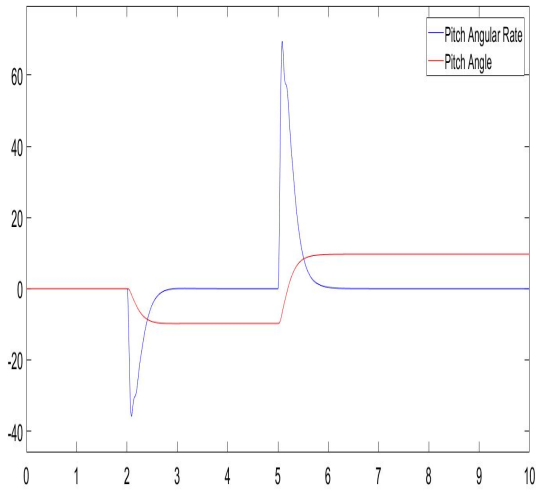

(b) Pitch Dynamics

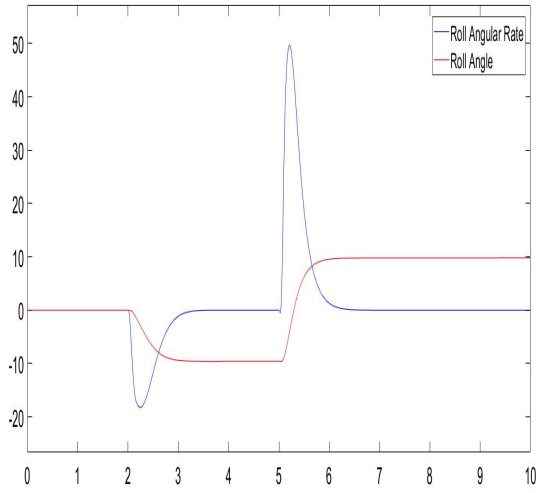

(c) Roll Dynamics

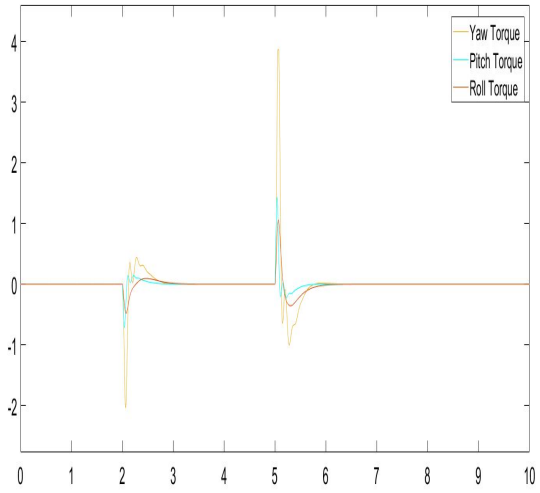

(d) Control Inputs

Figure 6.3: Hover Mode - Pitch Reference Input Tracking

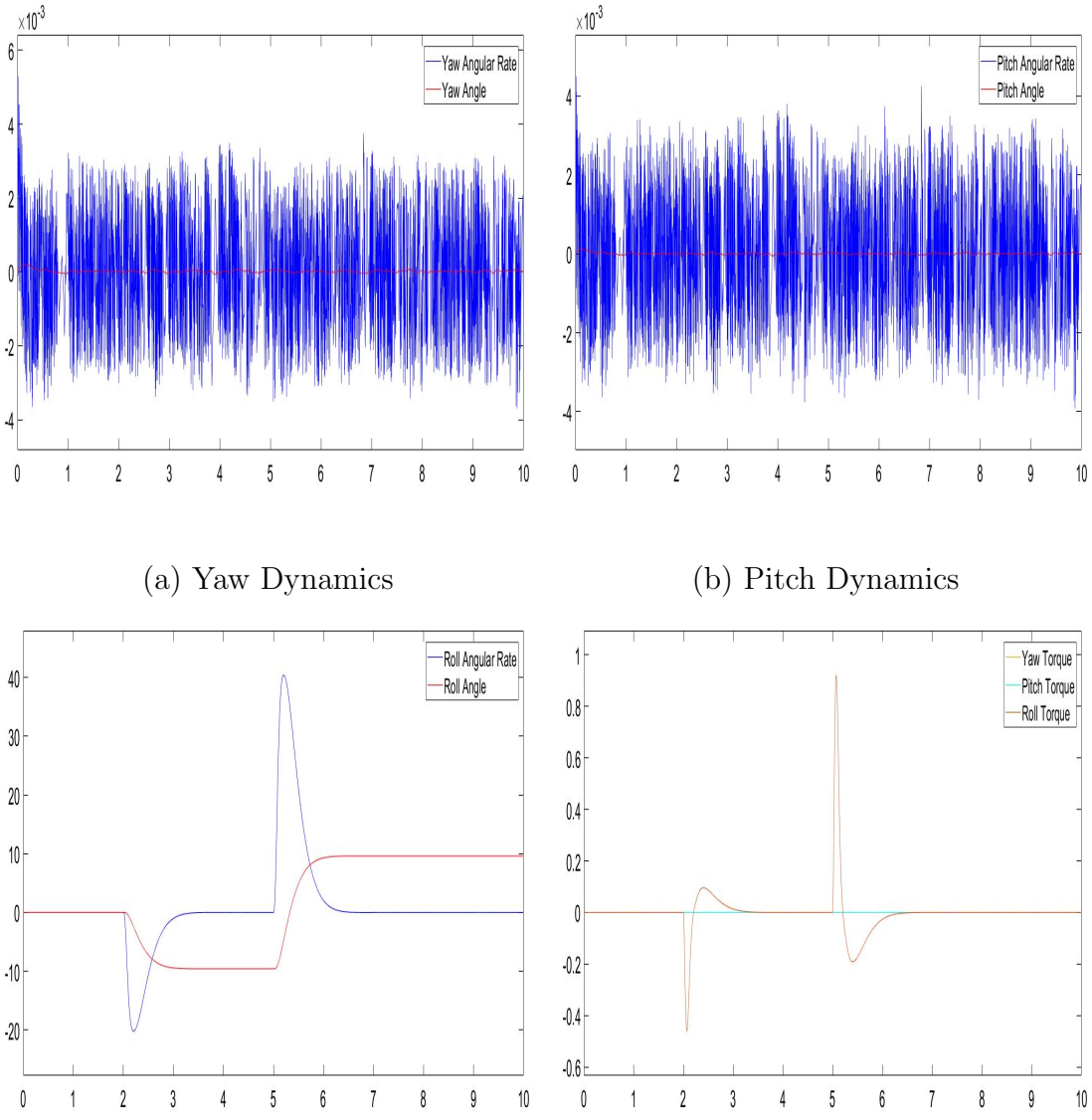

(a) Yaw Dynamics

(b) Pitch Dynamics

(c) Roll Dynamics

(d) Control Inputs

Figure 6.4: Hover Mode - Roll Reference Input Tracking

position. From the pitch down angle of 68 degrees until the horizontal flying position, the drone is operated at a rotational speed of 8000 rpm. An angle reference command of zero degrees is tracked by the closed loop yaw control system and the closed loop roll control system. A step change in pitch angle reference input from 0 degrees to -90 degrees is tracked by the closed loop pitch control system. The trajectories of the yaw angle, yaw angular rate, pitch angle, pitch angular rate, roll angle and the roll angular rate of the system are shown in Figure 6.5. The horizontal velocity of the drone during the transition flight from the hover to horizontal flying mode is shown in Figure 6.6. There can be a possibility of not achieving the minimum horizontal velocity called the stall velocity during the transition from hover to horizontal flight for a stable flight. During these situations, horizontal velocity can be gained by pitching down the drone from the horizontal flight and then getting the nose back up once the desired velocity is attained. The simulation of this maneuver is shown in Figure 6.7. For the purpose of payload delivery, we would require more thrust during hover take-off and in horizontal flight. In these cases, we should operate the drone at higher speeds to generate more thrust. To carry a payload of 0.5 kg, the drone would require operation at a speed of 9500 rpm in hover flight. During the hover to horizontal transition flight, the drone is maintained at 9500 rpm until the pitch down angle of 38 degrees. From the pitch down angle of 38 degrees until the pitch down angle of 68 degrees, the propellers are rotated at a speed of 9000 rpm. Then from the pitch down angle of 68 degrees until the horizontal flight, the drone is operated at a speed of 8500 rpm. The simulation results are shown in Figure 6.8. The horizontal velocity of the drone during the transition flight from hover to horizontal flying mode is shown in Figure 6.9. The pitching down maneuver during the horizontal flight for this set of speeds to gain horizontal velocity is shown in Figure 6.10.

The drone is operated at a speed of 10000 rpm in hover mode to handle a payload

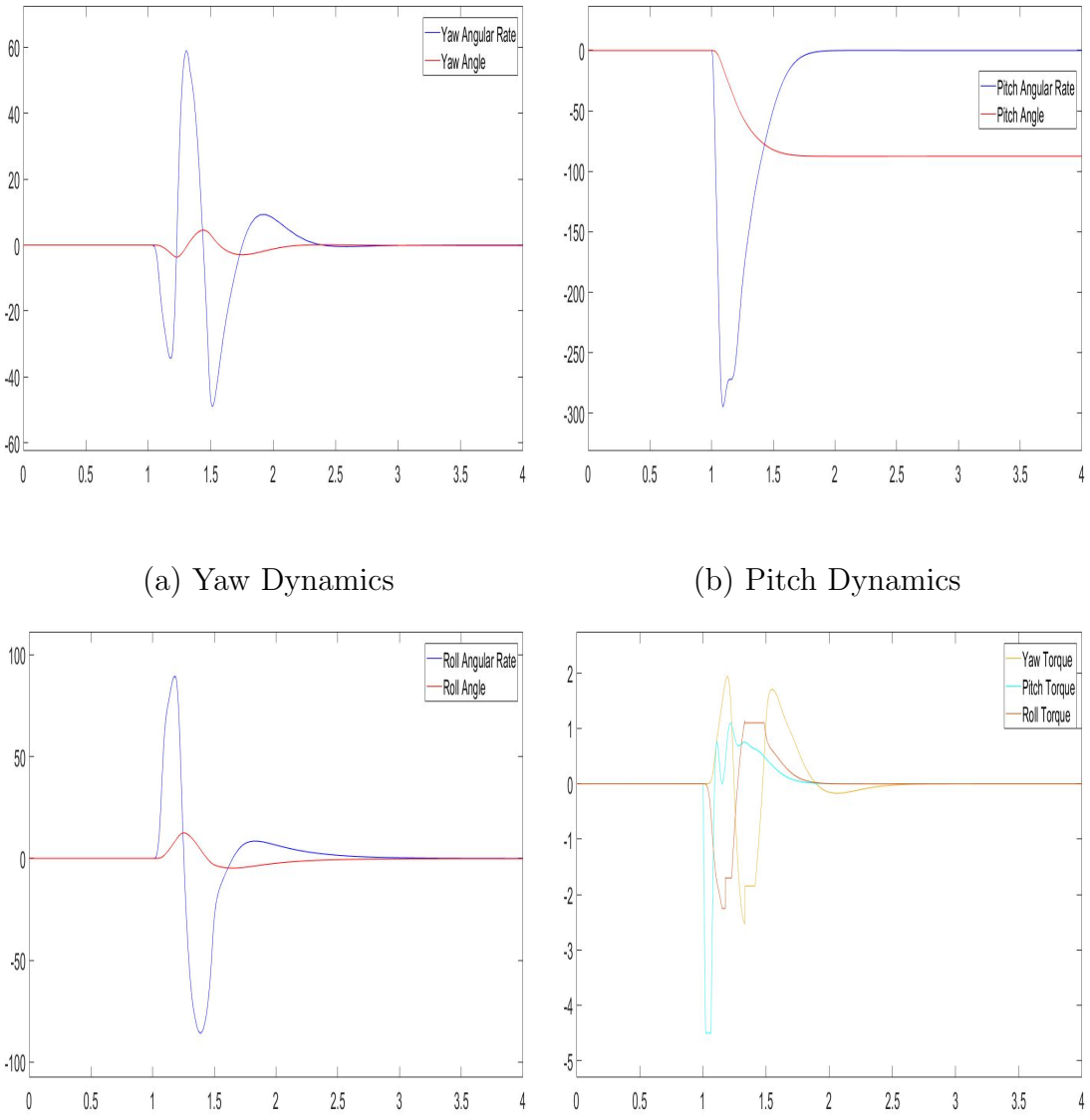

(a) Yaw Dynamics

(b) Pitch Dynamics

(c) Roll Dynamics

(d) Control Inputs

Figure 6.5: Hover to Horizontal Transition(Speeds of 9000, 8500, 8000 Rpm)

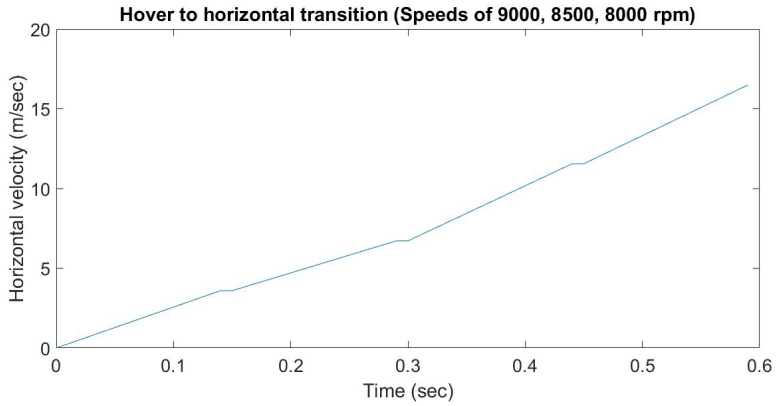

Figure 6.6: Horizontal Velocity During the Transition of the Drone from Hover to Horizontal Flying(Speeds of 9000, 8500, 8000 Rpm)

of 1kg.During the hover to horizontal transition flight, the plane is maintained at that speed until the pitch down angle of 38 degrees. From the pitch down angle of 38 degrees until the pitch down angle of 68 degrees, the drone is operated at 9500 rpm. From the pitch down angle of 68 degrees, until the horizontal flight, the propellers of the drone are rotated at a speed of 9000 rpm. The simulation results are shown in Figure 6.11. The horizontal velocity of the drone during the transition flight from hover to horizontal flying mode is shown in Figure 6.12. The pitching down maneuver for this set of speeds in operating the drone is shown in Figure 6.13.

6.3 Horizontal Flying Mode

The horizontal flight of the VTOL drone is simulated in SIMULINK in this section. The controllers designed for the linearized model of the drone about horizontal flying is tested on the non-linear dynamical model of the drone. The drone is operated at a rotational speed of 8000 rpm to generate adequate lift from the air flow over the airfoil shape of the wing. An unit step reference angle command is tracked by the closed loop yaw control system, closed loop pitch control system, closed loop roll

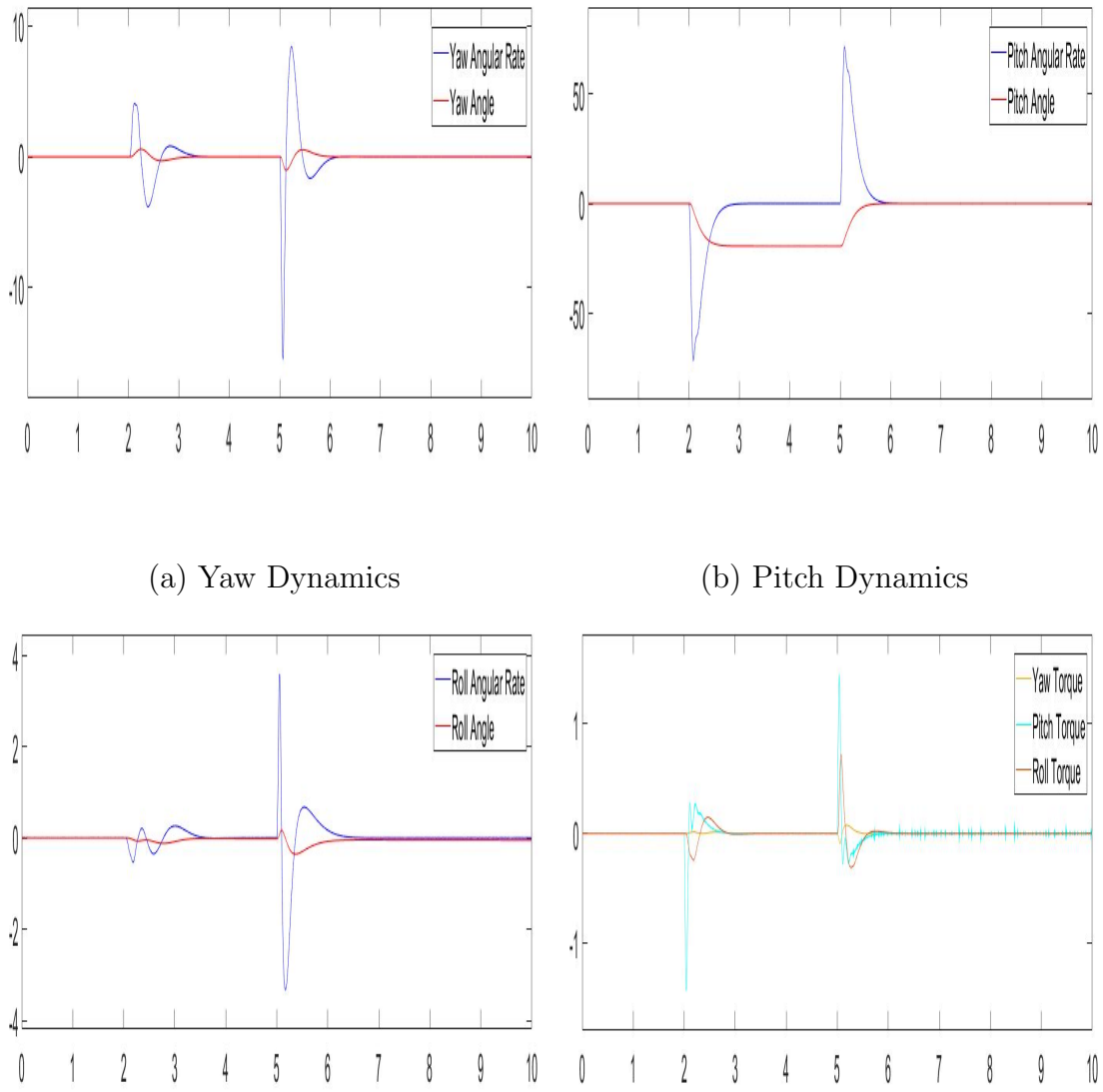

(a) Yaw Dynamics

(b) Pitch Dynamics

(c) Roll Dynamics

(d) Control Inputs

Figure 6.7: Horizontal Flight - Pitching down Maneuver for a Stable Horizontal Flight(Speeds of 9000, 8500, 8000 Rpm)

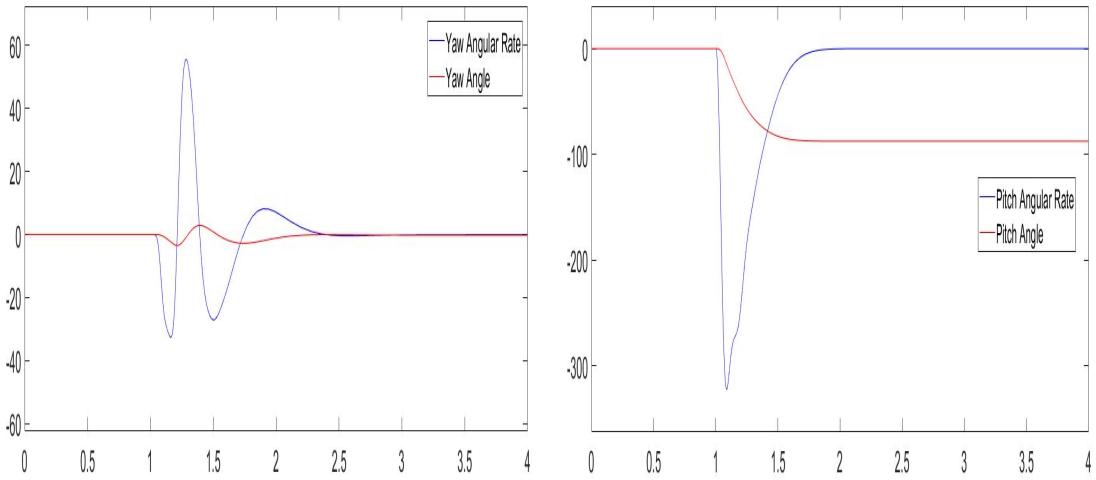

(a) Yaw Dynamics

(b) Pitch Dynamics

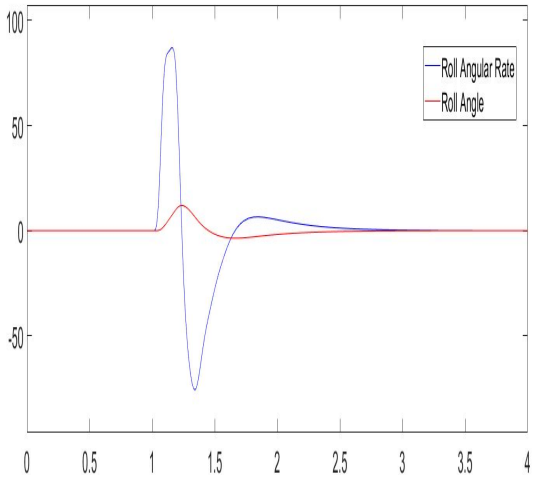

(c) Roll Dynamics

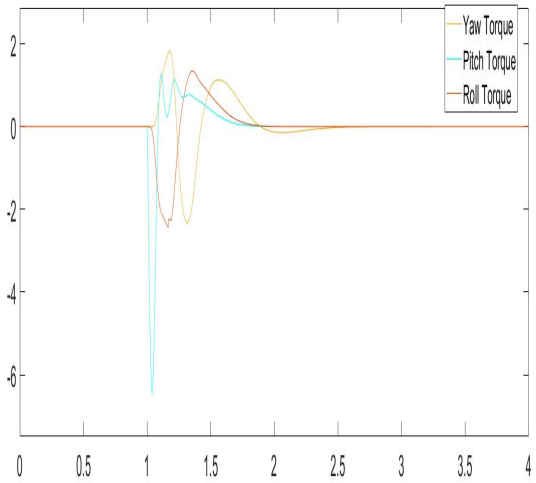

(d) Control Inputs

Figure 6.8: Hover to Horizontal Flight(Speeds of 9500, 9000, 8500 Rpm)

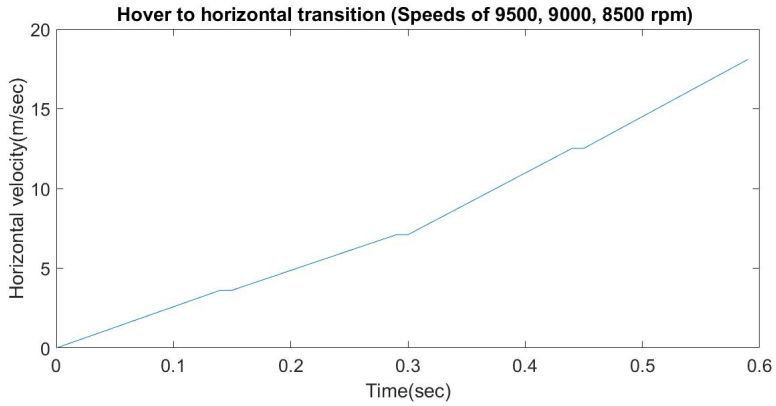

Figure 6.9: Horizontal Velocity During the Transition of the Drone from Hover to Horizontal Flying(Speeds of 9500, 9000, 8500 Rpm)

control system and the simulation results are shown in Figure 6.14. The reference tracking of the yaw control system with step changes in reference angle input is shown in Figure 6.15. The reference tracking of the pitch control system with step changes in reference angle input is shown in Figure 6.16. The reference tracking of the roll control system with step changes in reference angle input is shown in Figure 6.17.

6.4 Horizontal to Hover Flying Transition Mode

The horizontal to hover flying transition of the VTOL drone is simulated in SIMULINK in this section. The controllers designed for the linearized model of the drone about horizontal flying is tested on the non-linear dynamical model of the drone. The drone is operated at a rotational speed of 8000 rpm from the horizontal position until the pitch up angle of 38 degrees. Then the motor is rotated at a speed of 8500 rpm from the pitch up angle of 38 degrees until the pitch up position of 68 degrees. From the pitch up angle of 68 degrees until the hover flying position, the drone is operated at a rotational speed of 9000 rpm. A reference angle input of zero degrees is tracked by the closed loop yaw control system and closed loop roll control

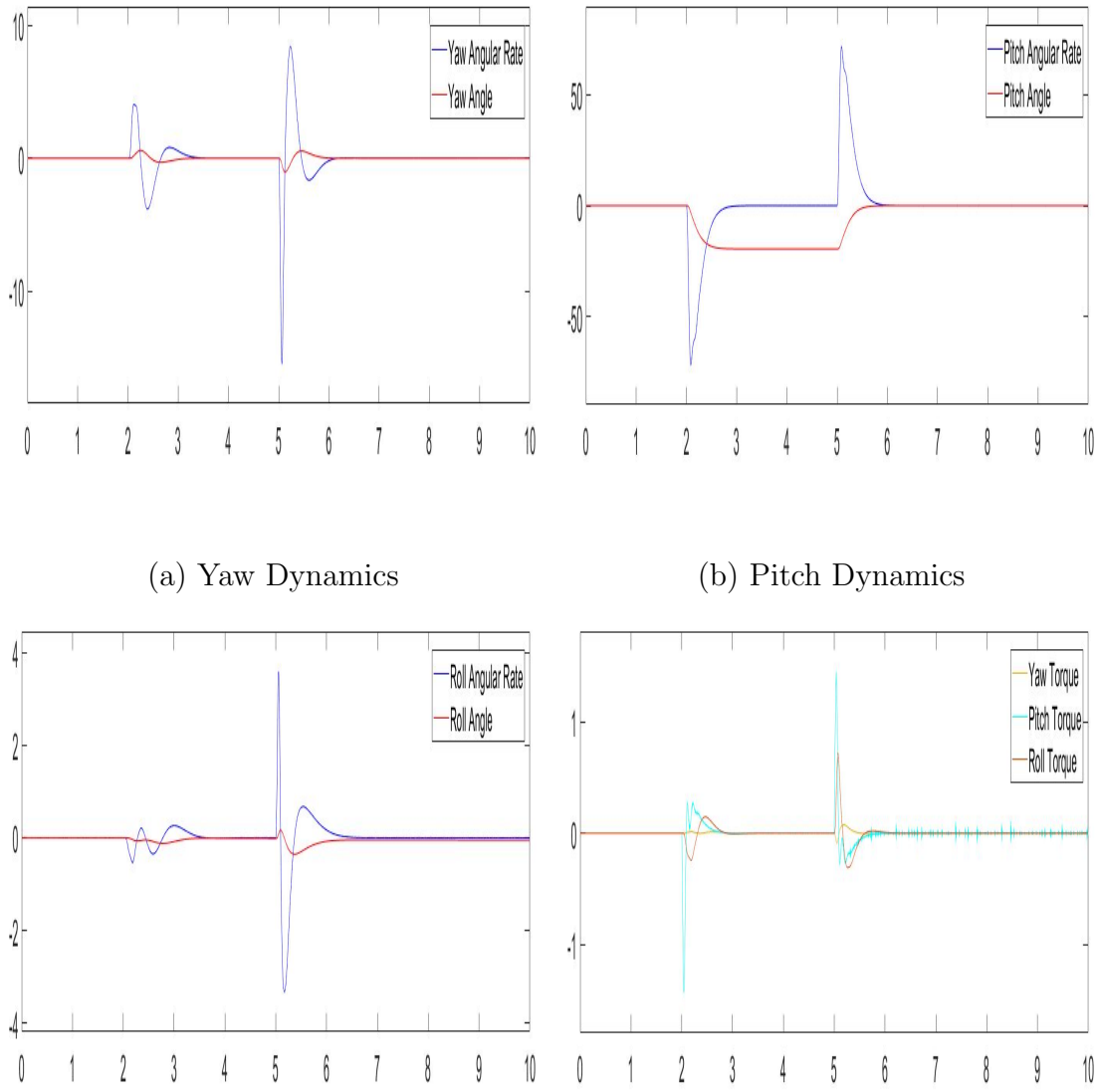

(a) Yaw Dynamics

(b) Pitch Dynamics

(c) Roll Dynamics

(d) Control Inputs

Figure 6.10: Horizontal Flight - Pitching down Maneuver for a Stable Horizontal Flight(Speeds of 9500, 9000, 8500 Rpm)

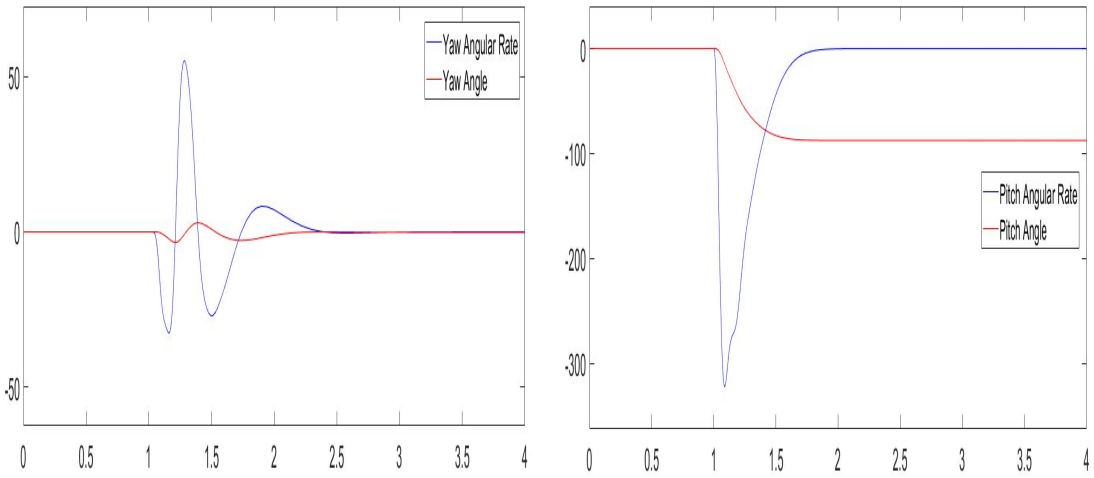

(a) Yaw Dynamics

(b) Pitch Dynamics

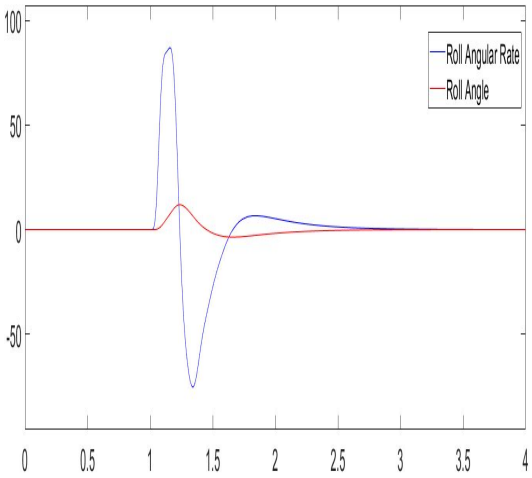

(c) Roll Dynamics

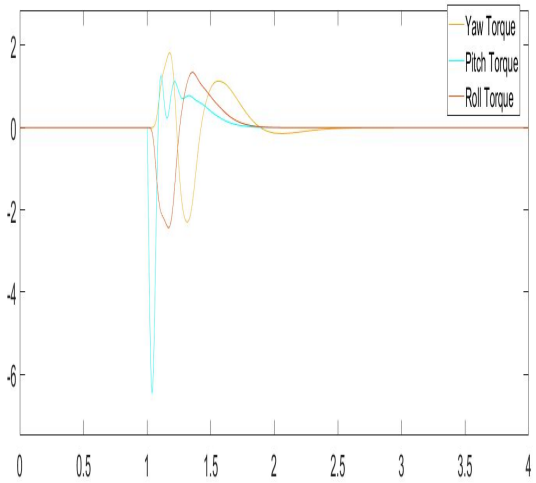

(d) Control Inputs

Figure 6.11: Hover to Horizontal Flight(Speeds of 10000, 9500, 9000 Rpm)

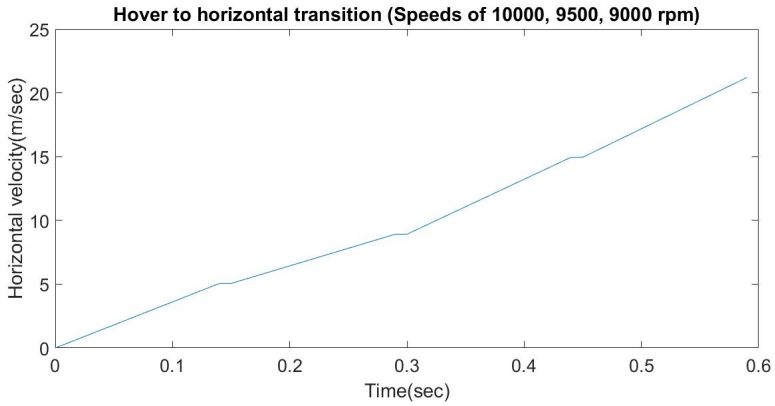

Figure 6.12: Horizontal Velocity During the Transition of the Drone from Hover to Horizontal Flying(Speeds of 10000, 9500, 9000 Rpm)

system. A step reference change from 0 degrees to 90 degrees of pitch angle is tracked by the pitch control system. The simulation results are shown in Figure 6.18. To carry a payload of 0.5 kg, the drone is operated at a speed of 8500 rpm during the horizontal flight. During the horizontal to hover transition flight, it is maintained at 8500 rpm until the pitch up angle of 38 degrees. From the pitch up angle of 38 degrees until the pitch up angle of 68 degrees, the propellers are rotated at a speed of 9000 rpm. Then from the pitch up angle of 68 degrees until the hover flight, the drone is operated at a speed of 9500 rpm. The simulation results are shown in Figure 6.19. To carry a payload of 1 kg, the drone is operated at a speed of 9000 rpm during the horizontal flight. During the horizontal to hover transition flight, the drone is maintained at 9000 rpm until the pitch up angle of 38 degrees. From the pitch up angle of 38 degrees until the pitch up angle of 68 degrees, the propellers are rotated at a speed of 9500 rpm. Then from the pitch up angle of 68 degrees until the hover flight, the drone is operated at a speed of 10000 rpm. The simulation results are shown in Figure 6.20.

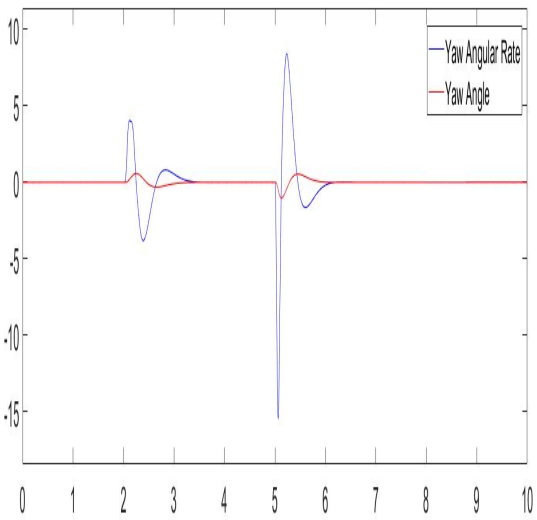

(a) Yaw Dynamics

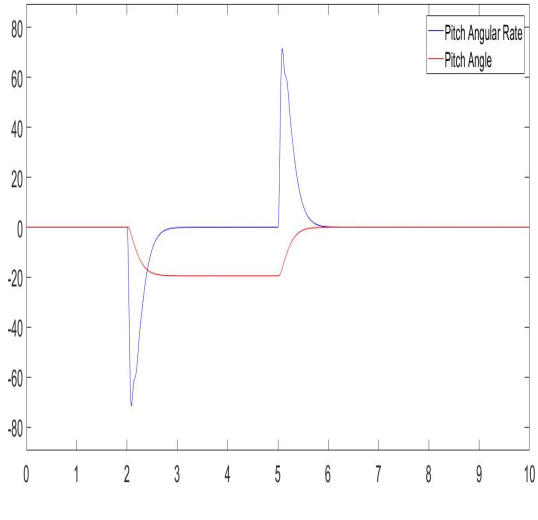

(b) Pitch Dynamics

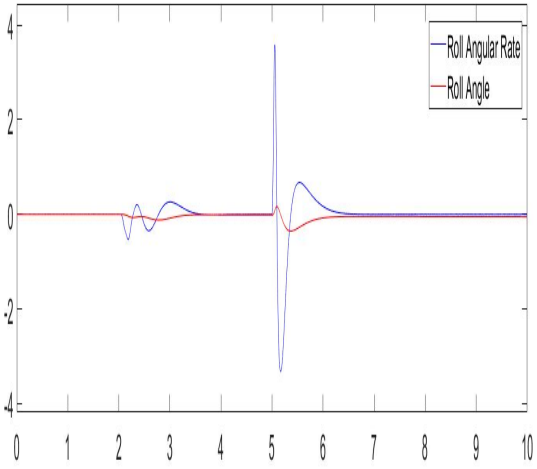

(c) Roll Dynamics

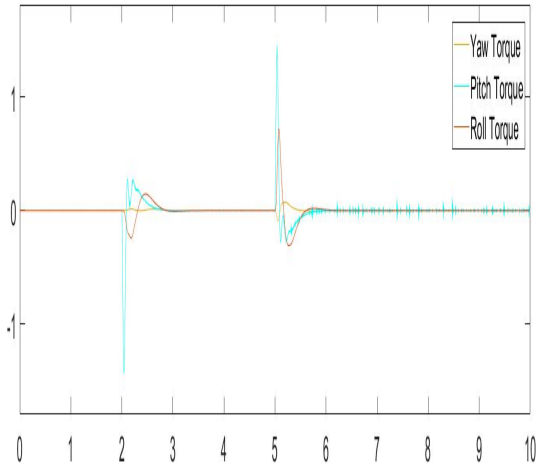

(d) Control Inputs

Figure 6.13: Horizontal Flight - Pitching down Maneuver for a Stable Horizontal Flight

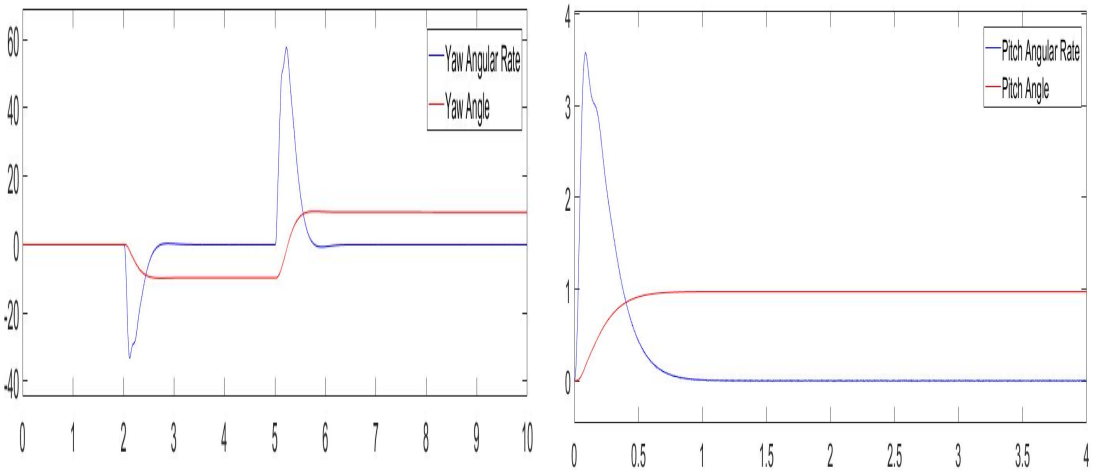

(a) Yaw Dynamics

(b) Pitch Dynamics

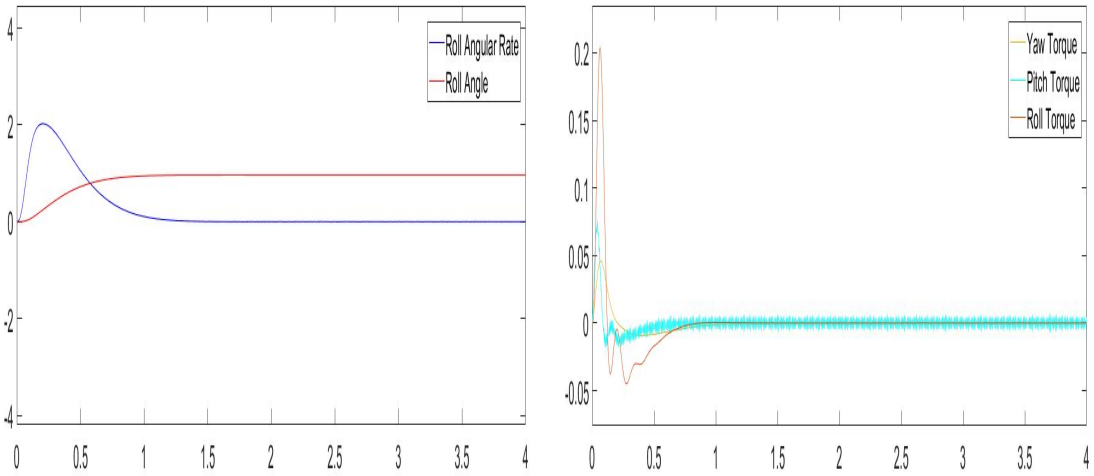

(c) Roll Dynamics

(d) Control Inputs

Figure 6.14: Horizontal Mode - Closed Loop Reference Tracking

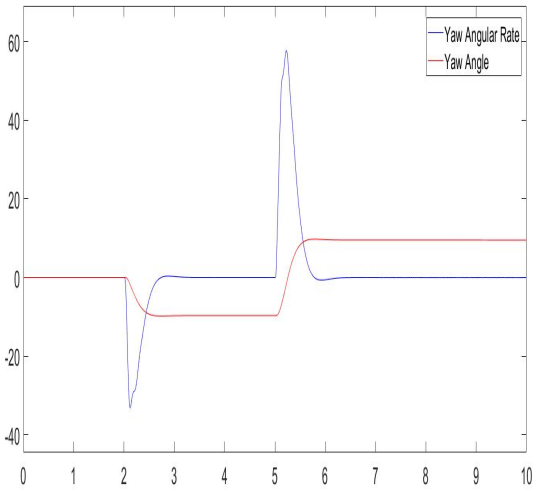

(a) Yaw Dynamics

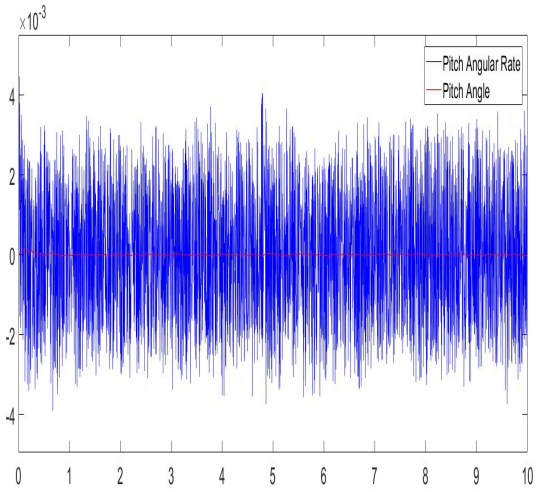

(b) Pitch Dynamics

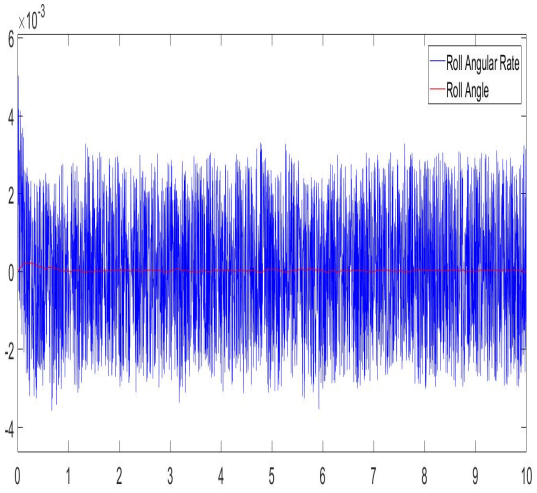

(c) Roll Dynamics

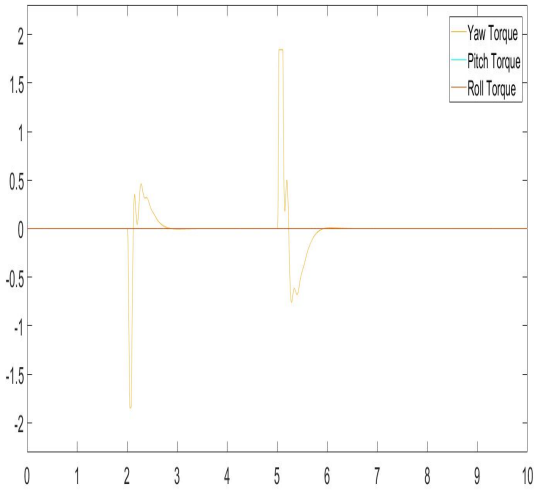

(d) Control Inputs

Figure 6.15: Horizontal Mode - Yaw Reference Input Tracking

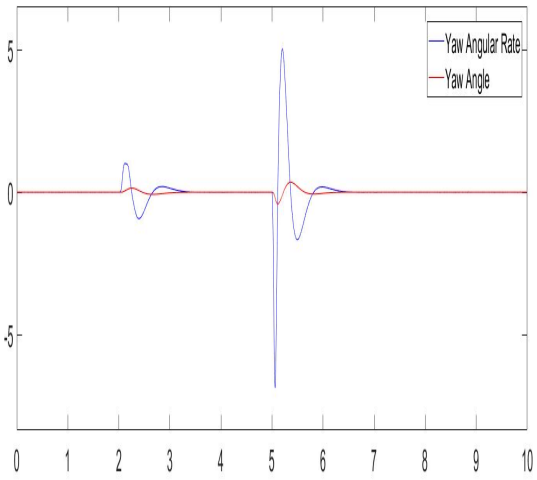

(a) Yaw Dynamics

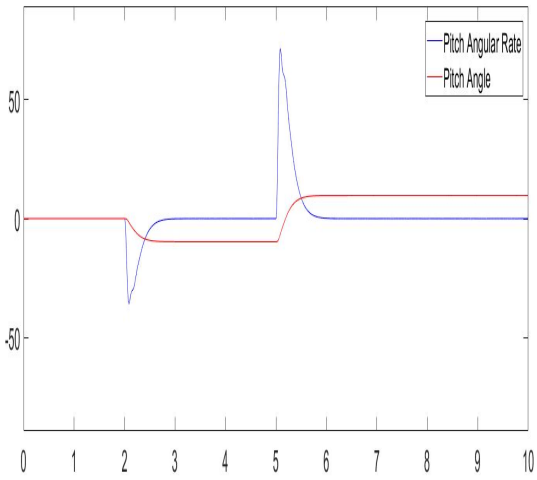

(b) Pitch Dynamics

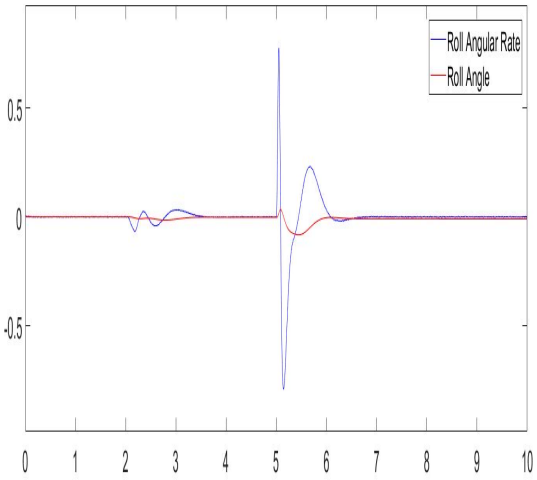

(c) Roll Dynamics

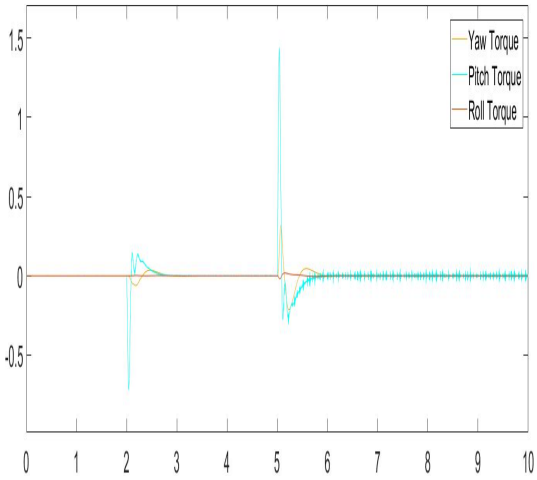

(d) Control Inputs

Figure 6.16: Horizontal Mode - Pitch Reference Input Tracking

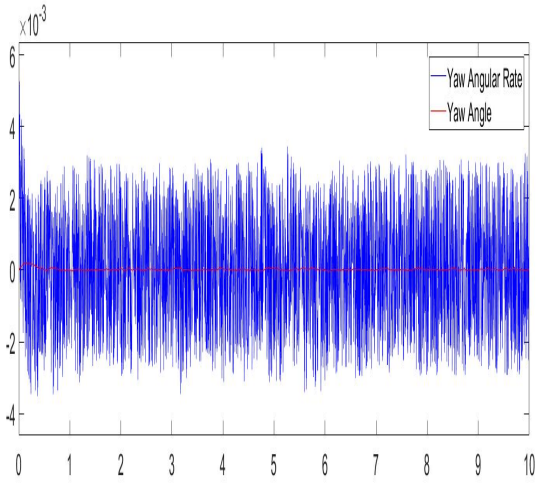

(a) Yaw Dynamics

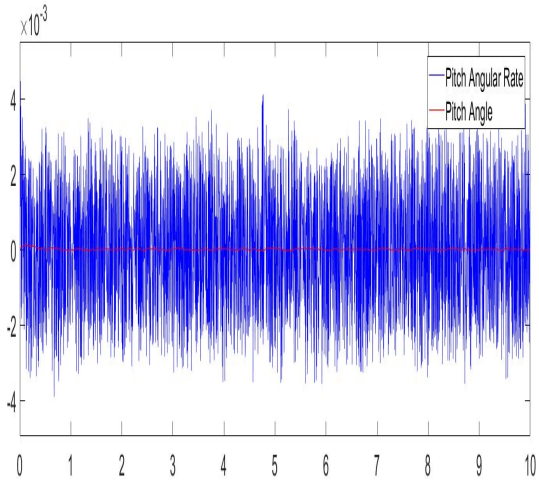

(b) Pitch Dynamics

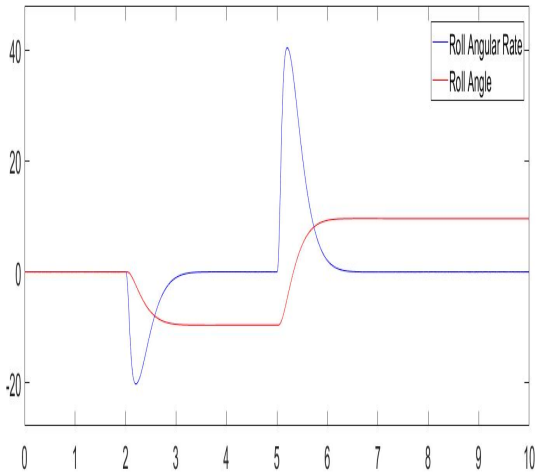

(c) Roll Dynamics

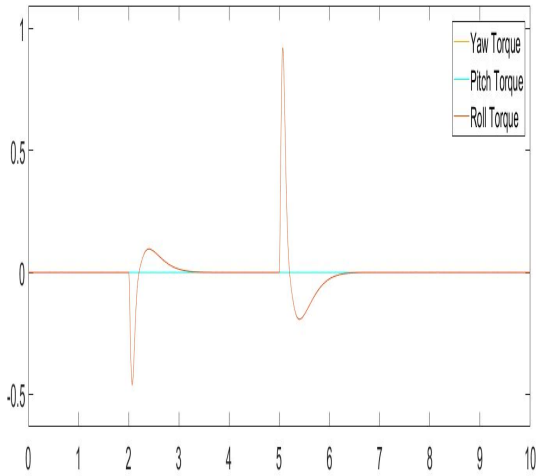

(d) Control Inputs

Figure 6.17: Horizontal Mode - Roll Reference Input Tracking

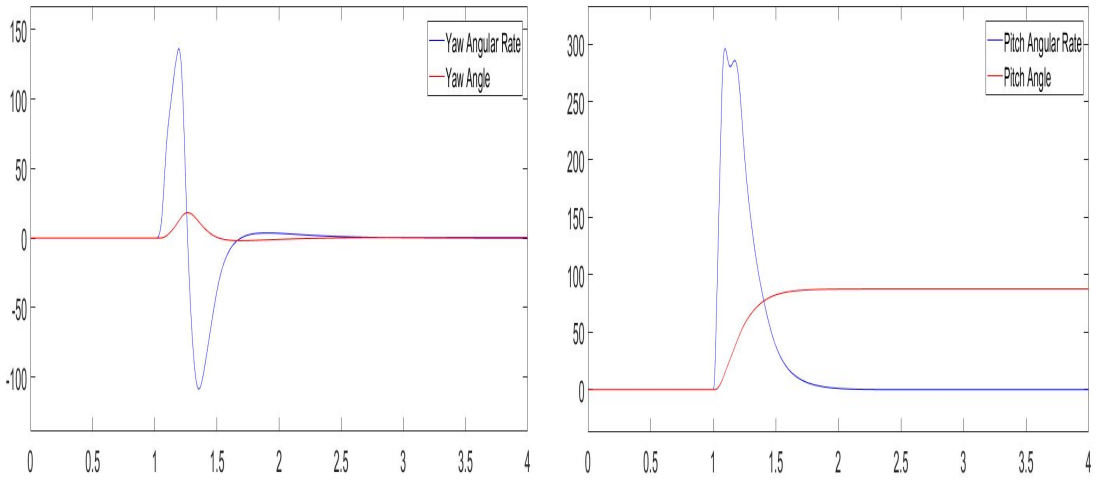

(a) Yaw Dynamics

(b) Pitch Dynamics

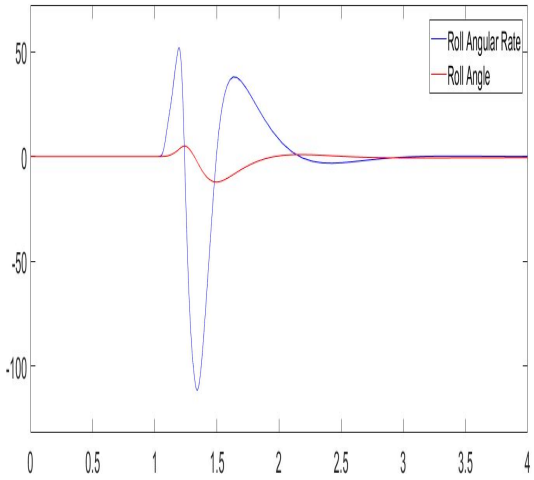

(c) Roll Dynamics

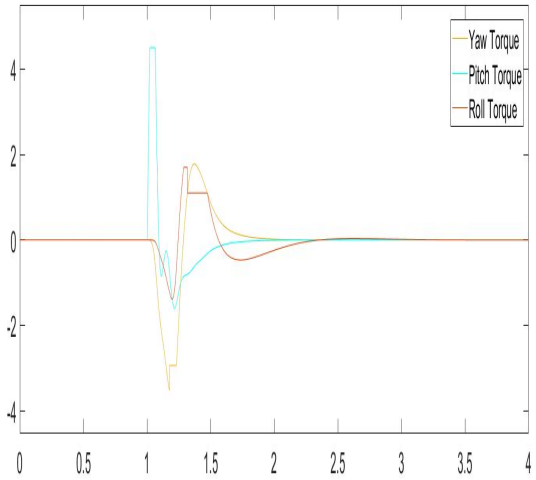

(d) Control Inputs

Figure 6.18: Horizontal to Hover Flight(Speeds of 8000, 8500, 9000 Rpm)

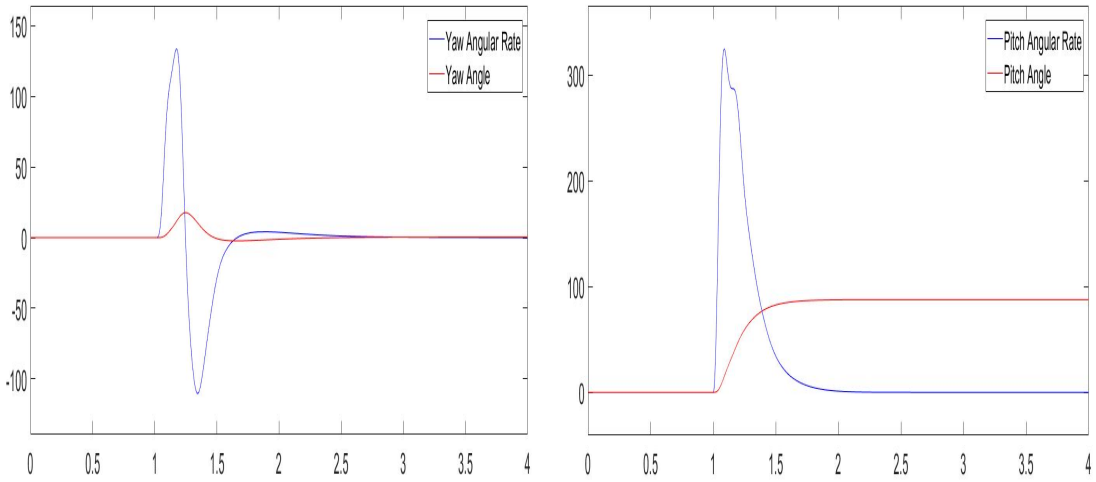

(a) Yaw Dynamics

(b) Pitch Dynamics

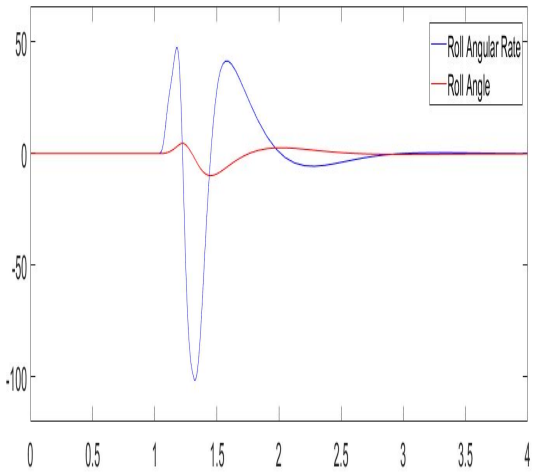

(c) Roll Dynamics

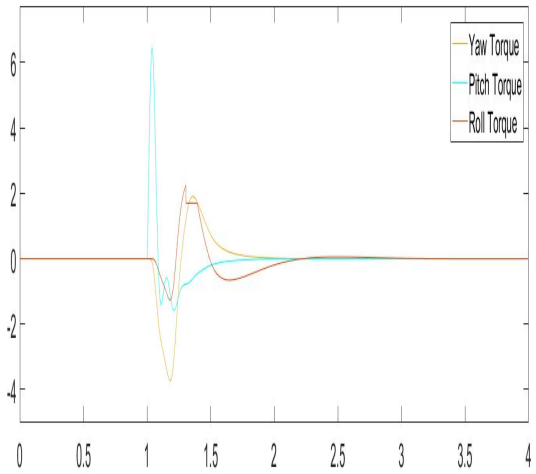

(d) Control Inputs

Figure 6.19: Horizontal to Hover Flight(Speeds of 8500, 9000, 9500 Rpm)

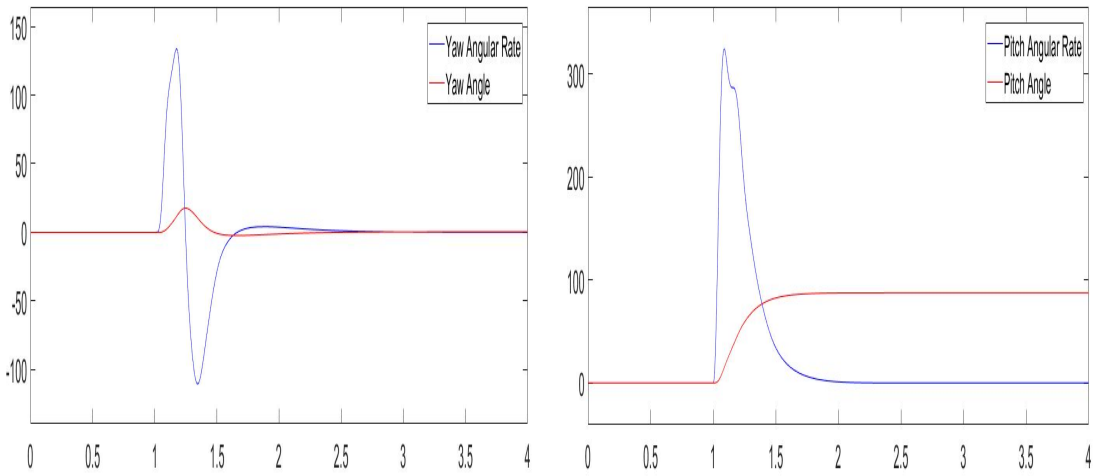

(a) Yaw Dynamics

(b) Pitch Dynamics

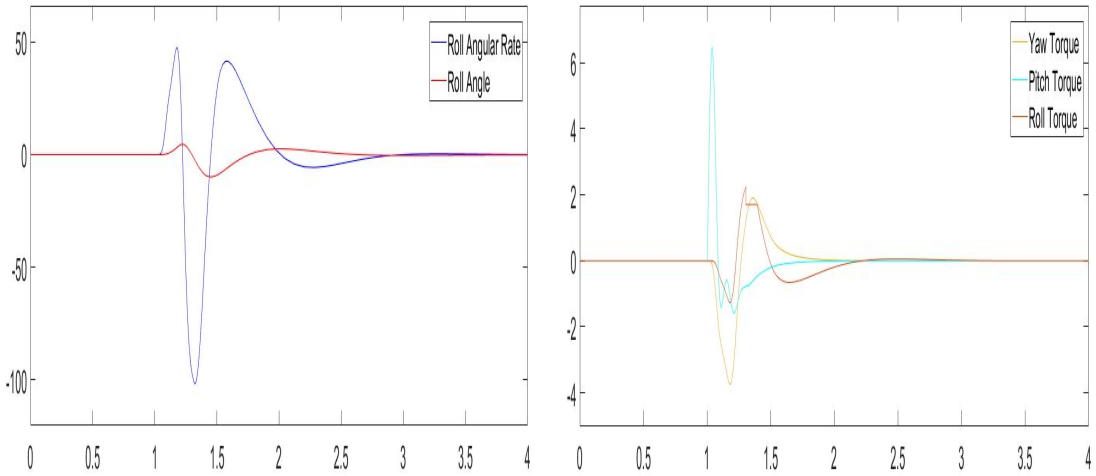

(c) Roll Dynamics

(d) Control Inputs

Figure 6.20: Horizontal to Hover Flight(Speeds of 9000, 9500, 10000 Rpm)

Chapter 7

CONCLUSION AND FUTURE WORK

7.1 Conclusion of Current Work

The motive of this project is to obtain a first principles model for the rotational dynamics- yaw, pitch, roll with inputs to the system being yawing torque, pitching torque, rolling torque and the outputs being yaw angle, pitch angle and roll angle respectively. The first principles model of the system completely reveals the behavior of the system along with its nonlinearities to help in implementing the hover to horizontal transition flight and the horizontal to hover transition flight. The nonlinear model of the drone is linearized about hover flying, horizontal flying for controller design through linear control design methodologies.

The linearized model of the drone about the corresponding operating points are utilized for controller design through a H_∞ loop shaping technique. A mixed sensitivity approach is used in controller design to define loop shapes for the sensitivity and the complementary sensitivity functions by defining weighting functions. The peak values of the sensitivity and complementary sensitivity functions are limited by the bounds specified for the weighting functions.

The hover flight of the drone is simulated with the control formulations and the yaw, pitch, roll reference angle inputs are tracked. Similarly, the hover to horizontal transition flight is simulated with changes in the rotational speeds of the motor and the yaw, pitch, roll dynamics are stabilized. The drone is operated at a higher velocity during the horizontal flight to have smooth air flow over its wings in-order to prevent the condition of stalling. At the same velocity, the horizontal flight of the drone

is simulated and the yaw, pitch, roll reference angle commands are tracked. Then, the horizontal to hover flight is simulated with the pitch angle changing from zero degrees to the hover flight position of 90 degrees and the yaw, pitch, roll dynamics are stabilized.

The theoretical analysis of different parameters of the drone are done to aid with the hardware implementation of the drone in real-time. The dynamical model of the brush-less dc motor is obtained by performing an experiment with an IR measurement setup to count the number of rotations per unit time. The thrust generated by the contra-rotating propellers are analyzed for different operational speeds of the brush-less dc motor. The rotation of the brush-less dc motor also generates a flow of slipstream underneath the cross-sectional area of the propellers which contributes the aerodynamic force for torque action during the yaw, pitch and roll rotation. The slipstream air velocity is analyzed for different speeds of operation of the brush-less dc motor. The torque acting on the system by the extension of the aileron control surfaces, rudder control surfaces are analyzed for different speeds of rotation of the contra-rotating propellers. With the above analysis, the torque to PWM input relation to aid in the precise deflection of control surfaces for a corresponding torque input from the control system is modeled.

Last, but not the least the experiment could be implemented with more confidence in the models with data obtained from the drone after initial implementation of the controllers. This would help in designing more accurate controllers to automate the flight of the drone.

7.2 Future Work

There is some amount of work to be done on this project. First, to obtain a precise model of the drone the aerodynamic analysis of the wings of the drone must be

done. The wing structure must be modeled in a computer automated drawing tool so that the airfoil analysis can be done by placing the wing design in a wind tunnel simulation environment. The velocity of slipstream that we would be experiencing during the flight of the drone is realized in the wind tunnel testing simulation, and the lift, drag force acting on the wing can be measured precisely to augment with the first principles model. This would result in a precise model of the drone with greater confidence in controller design stabilizing the physical system. The flight of the drone from hover to horizontal flight need to be implemented in hardware which would be successful with model augmentation from the airfoil analysis. With the new model, the linearized model could be obtained about different operating points during the hover to horizontal flight transition and gain scheduling technique could be incorporated to precisely control the system. Similarly, the horizontal flying model could be refined and the horizontal flight need to be implemented with the drone. The model of the drone about horizontal to hover flight of the drone should be obtained about different operating points during the transition and gain scheduling control should be implemented. Currently, we have a problem with wind disturbances affecting the flight of the drone. A wind estimation technique need to be incorporated to sense the wind and the controller must be capable of rejecting the wind disturbances. An automated landing of the drone should also be implemented for a safe landing. This project is to develop a first principles model to capture the nonlinearities in the dynamics of the drone and design controllers to stabilize the flight of the drone in hover flying, horizontal flying, hover to horizontal transition and horizontal to hover transition flight. We developed first principles model based on the physical model of the plane and its mass distribution. However, to precisely model the dynamics, experiments need to be conducted to obtain the aerodynamics of wings having the symmetric aileron control surfaces. The airfoil of the wing need to be modeled in a

computer design tool to perform wind tunnel testing of the airfoil for varying speeds of airflow over the wings for different speeds of rotation of the motor.

For the model obtained through first principles technique, we designed H_∞ loop shaped controllers guaranteeing robustness in the closed loop system performance and limiting the peaks of the sensitivity and complementary sensitivity functions for good low frequency command following, output disturbance and noise attenuation. The model of the drone need to be verified by implementing the controllers in real-time and if required, the model of the drone need to be refined. The flight of the plane need to be tested in hardware for the hover to horizontal transition, horizontal flying, horizontal to hover transition and analyze how the system behaves with respect to the simulated results. During the horizontal flying, smooth airflow over the wings must be ensured for a stable flight.

REFERENCES

[1] Y. Demitri, S. Verling, T. Stastny, A. Melzer and R. Siegwart, "Model-based Wind Estimation for a Hovering VTOL Tailsitter UAV" in 2017 IEEE International Conference on Robotics and Automation (ICRA) (IEEE 2017).

[2] Aidi Yang and Yong Wang, "A new VTOL Aircraft" in 2017 36th Chinese Control Conference , pp 6213-6218 (CCC,2017).

[3] Zhou, K., J. C. Doyle, K. Glover et al., "Robust and optimal control", vol. 40 (Prentice hall New Jersey, 1996).

[4] Van Overschee, P. and B. De Moor, "Subspace identification for linear systems: Theory Implementation and Applications" (Springer Science and Business Media, 2012).

[5] Tsakalis, K. and P. Ioannou, "Linear time varying systems: Control and Adaptation prentice-hall", Englewood Cliffs, NJ (1993).

[6] Stoorvogel, A. A., "The H_∞ Control Problem: A State Space Approach" (Prentice Hall.,1992).

[7] Qin, S. J., "An overview of subspace identification", Computers and chemical engineering 30, 10, 15021513 (2006).

[8] Hassan Khalil, "Nonlinear control systems" (Prentice Hall, 2002).

[9] McRuer, D. T., D. Graham and I. Ashkenas, "Aircraft dynamics and automatic control" (Princeton University Press, 2014).

[10] McFarlane, D. and K. Glover, "A loop-shaping design procedure using H_∞ synthesis", Automatic Control, IEEE Transactions on 37, 6, 759769 (1992).

[11] Bouabdallah, S., P. Murrieri and R. Siegwart, "Design and control of an indoor micro quadrotor", in Robotics and Automation, 2004. Proceedings. ICRA04 2004 IEEE International Conference on, vol. 5, pp. 43934398 (IEEE, 2004).

[12] Lecture Slides of "MAE 313 Aircraft Dynamics and Control" by Dr. Matthew Monnig Peet taught at "Illnois Institute of Technology".

[13] Haowei Gu, Ximin Lyu, Zexiang Li, Shaojie Shen, and Fu Zhang, "Development and Experimental Verification of a Hybrid Vertical Take Off and Landing (VTOL) Unmanned Aerial Vehicle (UAV)", in International Conference on Unmanned Aircraft Systems, pp. (160 - 169) (ICUAS, 2017).

[14] Naidu, D. S., "Optimal control systems" (CRC press, 2002).

[15] Li Xiaocheng; Wang Jingcheng; Lin Hai; Zhang Yeming; Jiang Huaide; Yuan Yi; Ji Yong; Liu Yan; Chen Yang; Wang Quan; Sun Huibin, "Adaptive controller decomposition bumpless transfer for switching control" in "2017 Chinese Automation Conference(CAC)".

[16] David J. Hoelzle; Amy J. Wagoner Johnson; Andrew G. Alleyne, "Bumpless Transfer Filter for Exogenous Feedforward Signals" in IEEE Transactions on Control Systems Technology (IEEE, 2014).

[17] Nagore Iriondo; Marga Marcos; Elisabet Estvez, "Bumpless transfer multi controller architecture for switched mode processes" in Proceedings of 2012 IEEE 17th International Conference on Emerging Technologies and Factory Automation (ETFA

2012).

[18] W. Bao; Y. Qi; J. Zhao; J. Chang , "Robust dynamic bumpless transfer: an exact model matching approach" in IET Control Theory and Applications(IET 2012).

[19] Yiwen Qi; Wen Bao , "Dynamic bumpless transfer: An exact model matching approach" in Proceedings of the 30th Chinese Control Conference, IEEE 2011.

[20] I. Malloci; L. Hetel; J. Daafouz; C. Iung; R. Bonidal , "Bumpless transfer for discrete-time switched systems" in 2009 American Control Conference.

[21] Joel Steenis; Kostas Tsakalis; Raja Ayyanar, "An Approach to Bumpless Control for LPV Modeled Inverters in a Microgrid" in IEEE Transactions on Power Electronics.(IEEE 2014).

[22] F. J. Jeffy; Anuj Abraham; N. Pappa,"Decoupler design using dynamic state feedback approach for a binary distillation column" in 2017 Trends in Industrial Measurement and Automation (TIMA).

[23] B. J. Parvat; B. M. Patre, "Design of SMC with decoupler for multi-variable coupled tank process" in 2014 Annual IEEE India Conference(INDICON).

[24] Jin Qibing; Huang Wenbing, "Tuning Algorithm of an Internal Model Control Decoupler" in 2010 International Conference on Electrical and Control Engineering.

[25] Devi C. Arati; S. Narayanan , "Dynamic decoupling design for a class of linear multivariable system" in 2015 International Conference on Computer, Communication and Control (IC4).

[26] Devi C. Arati; S. Narayanan; N. Sivakumaran ."Complete decoupling of multivariable systems by means of dynamic state feedback" in 2015 International Conference on Smart Technologies and Management for Computing, Communication, Controls, Energy and Materials (ICSTM).

[27] S. Sundari; Alamelu Nachiappan , "Decoupling based control analysis of a continuous stirred tank reactor (CSTR)" in 2017 International Conference on Innovative Research In Electrical Sciences (IICIRES).

[28] MIT Open CourseWare, course on "Dynamics".

[29] Bzioui Sana; Channa Rafik, "Robust H-infinity tracking control of MIMO nonlinear systems. Application to non-isothermal CSTR", 2017 International Conference on Control, Automation and Information Sciences (ICCAIS).

[30] Gerasimos Rigatos; Pierluigi Siano; Masoud Abbaszadeh; Sul Ademi, "Nonlinear H-infinity control for the rotary pendulum", 2017 11th International Workshop on Robot Motion and Control (RoMoCo).

[31] Gonzalo A. Garcia; Shawn Kashmiri; Daksh Shukla, "Nonlinear control based on H-infinity theory for autonomous aerial vehicle", 2017 International Conference on Unmanned Aircraft Systems (ICUAS).

[32] Muhammad Imran Ullah; Syed Ali Ajwad; Muhammad Irfan; Jamshed Iqbal ,"MPC and H-Infinity Based Feedback Control of Non-Linear Robotic Manipulator", 2016 International Conference on Frontiers of Information Technology (FIT).

[33] Razvan C. Rafaila; Gheorghe Livint , "H-infinity control of automatic vehicle steering", 2016 International Conference and Exposition on Electrical and Power En-

gineering (EPE).

[34] Diego Navarro-Tapia; Andres Marcos; Samir Bennani; Christophe Roux , "Structured H-infinity control based on classical control parameters for the VEGA launch vehicle", 2016 IEEE Conference on Control Applications (CCA).

[35] K. Vinida; Mariamma Chacko, "A novel strategy using H infinity theory with optimum weight selection for the robust control of sensorless brushless DC motor" , 2016 IEEE Symposium on Sensorless Control for Electrical Drives (SLED).

[36] N. H. Chalidia; M. Nuh; E. A. K. Rusdhianto , "Autonomous VTOL design in quadcopter using feedback linearization and fuzzy T-S", 2017 International Conference on Control, Electronics, Renewable Energy and Communications (ICCREC).

[37] Gerasimos Rigatos; Pierluigi Siano , "An H infinity feedback control approach to autonomous robot navigation", IECON 2014 - 40th Annual Conference of the IEEE Industrial Electronics Society.

[38] "Nonlinear control based on H-infinity theory for autonomous aerial vehicle", Gonzalo A. Garcia; Shawn Kashmiri; Daksh Shukla, 2017 International Conference on Unmanned Aircraft Systems (ICUAS).

[39] Omar Aedo; Karina. A. Barbosa; Arturo lvarez , "Mixed controller design for an UAV flight control system", 2015 CHILEAN Conference on Electrical, Electronics Engineering, Information and Communication Technologies (CHILECON).

[40] Fucheng Cao; Xianwei Wang; Jixia Shi, "Robust H-Infinity Control of Intelligent Autonomous Navigation Wheelchair", 2013 IEEE 9th International Conference on Mobile Ad-hoc and Sensor Networks.

[41] Gonzalo A. Garcia; Shahriar Keshmiri; Richard D. Colgren, "H-Infinity gain scheduling design for the meridian UAS for a broader range of operation and for fault tolerant applications", 2011 9th IEEE International Conference on Control and Automation (ICCA).

[42] Jemie Muliadi; Rizki Langit; Benyamin Kusumoputro, "Estimating the UAV moments of inertia directly from its flight data", 2017 15th International Conference on Quality in Research (QiR): International Symposium on Electrical and Computer Engineering.

[43] Jian Zhang, Yongpeng Zhang, Warsame Ali, Leang-san Shieh, "Linearization modeling for non-smooth dynamical systems with approximated scalar sign function" in 2011 50th IEEE Conference on Decision and Control and European Control Conference.

[44] E.Grassi, K.Tsakalis, "PID controller tuning by frequency loop-shaping: application to diffusion furnace temperature control" in IEEE Transactions on Control Systems Technology 2000.

[45] Shafique A.B, K.Tsakalis,"Discrete-Time PID Controller Tuning Using Frequency Loop-Shaping" in IFAC Conference on Advances in PID Control 2012.

[46] E.Grassi, K.Tsakalis, S. Dash, S. V. Gaikwad, W. MacArthur, G. Stein, "Integrated system identification and PID controller tuning by frequency loop-shaping" in IEEE Transactions on Control Systems Technology 2001.

[47] Armando Rodriguez, Textbook on "Design of multi-variable control systems"